Analyzing defects and their effects on the strength of a three-layer FSW joint by using X-ray microtomography, localized spectrum analysis, and acoustic emission

E.L. Nitu, M. Diakhaté, C. Badulescu, M. Grédiac, B. Blaysat, D.M. Iordache, A. Bosneag, J. Adrien, E. Maire, Matthieu Dhondt, et al.

Analyzing defects and their effects on the strength of a three-layer FSW joint by using X-ray microtomography, Localized Spectrum Analysis, and Acoustic Emission

E. L. Nitu[a], M. Diakhaté[b], C. Bădulescu[c*], M. Grédiac[d], B. Blaysat[d], D. M. Iordache[a], A. Bosneag[a], J. Adrien[e], E. Maire[e], M. Dhondt[c], and Y. Demmouche[c]

[a]*Manufacturing and Industrial Management Department, University of Pitesti, Pitesti, Romania;*

[b]*IRDL-UMR CNRS 6027, Univ. Bretagne Occidentale, F-29600 Morlaix, France ;*

[c]*IRDL-UMR CNRS 6027, ENSTA Bretagne, F-29200 Brest, France;*

[d]*Institut Pascal, UMR 6602, Université Clermont Auvergne, CNRS, SIGMA Clermont Institut Pascal, Clermont-Ferrand, France*

[e]*UMR CNRS 5510, Laboratoire MATEIS, University Lyon, INSA Lyon, Villeurbanne, France*

*corresponding author

Claudiu Bădulescu, *claudiu.badulescu@ensta-bretagne.fr*

Abstract

The present work aims at proposing an experimental strategy involving three measurement techniques, namely X-ray micro-computed tomography, Localized Spectrum Analysis, and Acoustic Emission (AE) in order to detect the initiation of damage mechanisms within an FSW joint and to track its evolution during a mechanical test. The specimen was manufactured by superimposing and welding together three aluminum alloy sheets named AA6061, AA7075, and AA2024. First, the defects within the internal structure of the joint were identified by using X-ray micro-computed tomography. The joint was then subjected to a tensile test. The evolution of the defects as a function of the tensile stress was monitored by using acoustic emission coupled with non-contact strain fields measurements on two perpendicular faces of the specimen. The findings highlight a good correlation between the strain-concentration zones and those characterized by a high density of weld defects, as identified from the analysis of the microtomography results. The comparison between AE results with those obtained from the computed microtomography analysis enabled us to state that the first crack sources were caused by the weakness zones detected within the initial state of the welded joint. The findings from an unsupervised classification of the AE activity are

that three main mechanisms governed the damage evolution of the studied FSW joint. The acoustic signature of each cracking mechanism is defined by a pair of values (peak frequency, amplitude), each within a specific range. A deep analysis of the experimental results highlights a good correlation between the AE results with those from the strain analysis.

Keywords: Friction stir welding; X-ray micro-computed tomography; Localized spectrum analysis; Acoustic emission; Aluminum alloy

1) Introduction

The major challenge today mainly focuses on the reduction of energy consumption in different economic sectors. The conversion of energy significantly affects our environment and leads to high levels of air pollution. As an example, transport is the activity that contributes to most of the greenhouse gas emissions in France since it was estimated in 2019 at around 31% of the whole emissions [1]. Based on this observation, the design of mechanical structures in the transport industry should lead to a high strength/weight ratio [2]. Indeed, the use of these structures is an effective way to reduce the total weight of future vehicles, thus improving energy efficiency while reducing fuel consumption [3]. These structures are obtained by assembling different materials which are characterized by both a lightweight and a high mechanical strength. Such materials are generally difficult to weld and thus are conventionally joined by riveting, bolting, or screwing. One disadvantage of these joining processes is that they increase the weight of the assembly. An alternative to these assembling processes is the friction stir welding (FSW) technique. The latter was invented and patented by The Welding Institute (TWI) [4]. This is solid-state welding characterized by a low heat generation and a welding temperature lower than the fusion one of the materials involved in the joint. Because of the insignificant thermal distortions generated by the FSW process [5], the latter is suited for welding dissimilar materials. Many studies showed that the FSW technique is well suited for assembling similar or dissimilar materials [6] by using either the lap joint [7] or the butt-joint method. Some recent studies have addressed welded joints made up of two superimposed sheets using the FSW process by performing several welding passes [8, 9] and by varying the depth value of the welding tool. Welding defects were observed from the result analysis. However, their number, as well as their distribution, were not quantitatively evaluated. These defects could be of tunneling and kissing bond types [10] or pore types [11] that are specific to welding configurations of superimposed sheets.

The appearance of defects within this welding configuration is one of the most important issues because the heat generated by the friction between the shoulder of the pin and the alloy sheet is not always homogeneously spread at the interlayer between sheets. Another reason is that the values of both the mechanical and the thermal properties of the sheets being welded are generally different. Considering these experimental conditions involves choosing the joining parameters (advancing speed and rotational speed) in such a way that an optimal welding temperature is obtained in the stir zone [12]. This also ensures the strongest interface between the welded sheets and minimizes the creation of defects in the joint.

Compared to the studies mentioned above in which two superimposed and welded sheets were investigated, an FSW joint made of three superimposed steel sheets was investigated in [13] to understand the effect of the direction of the tool rotation on the joint quality, especially in terms of the formation of hooking defects [14]. Three ultra-thin aluminum alloy sheets, each having a thickness of 0.254 mm [15], were superimposed and welded by using micro friction stir welding before being experimentally tested. The authors were able to demonstrate that the shape of the tool highly affects the joint strength and that the creation of defects during the welding process can be minimized by selecting appropriate welding parameters. Nevertheless, few studies focus on quantifying these defects as well as their effect on the in-service life of FSW joints obtained by superimposing metal sheets. Recently, some authors [11,16] have successfully detected defects within FSW joints by using non-destructive testing such as X-ray micro-computed tomography (CT). Moreover, the authors have highlighted the dependency between the welding process parameters and the resulting number of defects. As a general conclusion of this brief bibliography, there is a need for coupling several experimental techniques to better understand the evolution of the defects in FSW joints as well as their effect on the in-service life of the joints when subjected to mechanical loading.

While the heterogeneity in the vicinity of the welded zone can be analyzed through strain fields measurements on the specimen surfaces [17,18], it is more difficult to investigate the internal structure of the joint, particularly when focusing on the identification of the damage mechanisms [19]. For this purpose, the acoustic emission [20, 21] is a suitable technique for monitoring the creation of defects within the welded joint but also for identifying the acoustic signatures that could be associated with each of the damage mechanisms.

The present work aims at proposing an experimental strategy involving three different complementary measurement techniques (X-ray micro-computed tomography, Localized Spectrum Analysis, and Acoustic Emission), the main objective being to detect both the

initiation and the evolution of damage mechanisms within an FSW joint. These three techniques were chosen because of their non-destructive and non-contact nature (except the acoustic emission). They also provide full-field measurements, which leads to a wealth of data. This turns out to be useful to understand the mechanisms that govern the mechanical behavior of the joint. Moreover, the synchronization of these three techniques enabled us to correlate the results that they provided. First, the defects within the internal structure of the joint were identified by using X-ray micro-computed tomography before subjecting the joint to tensile loading. The evolution of these defects as a function of the applied tensile stress was monitored by using acoustic emission coupled with non-contact strain fields measurements on two perpendicular faces of the specimen. These faces were marked with periodic patterns such as checkerboards to ensure a high quality of the displacement and strain fields measurement. This technique also aimed at detecting very early the appearance of strain concentrations on the two investigated surfaces of the specimen. The originality of this work is mainly the fact that the three experimental techniques which were used provided complementary information. This enabled us to investigate in detail a complex welding configuration. This would not have been the case if they had been employed separately.

2) Materials and Experimental Methods

2.1 Specimen preparation

Figure 1 provides an overview of the studied specimen as well as the size of the zones under investigation. In this experimental study, (as shown in Figure 3) three aluminum alloy sheets designated AA6061, AA7075, and AA2024 were superimposed in this order and welded together by using the FSW process. The initial size of each alloy sheet is 250 mm in length, 140 mm in width, and 2 mm thick. Once the sheets were welded, the specimen to be tested was cut by machining from a region where the FSW process could be considered as stabilized (i.e. roughly 70 mm away from the edge of the initial sheets), the measured welding temperature remaining constant and being no longer influenced by the welding tool (pin) advance.

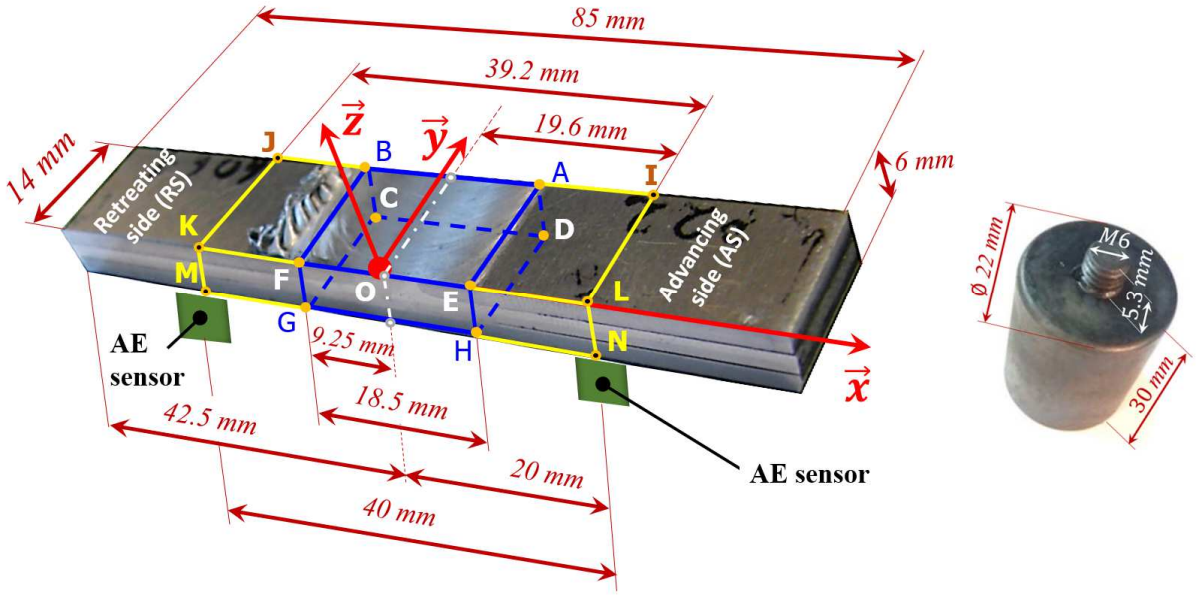

Figure 1 - Geometry of the FSW specimen with details of the investigated areas and the tool

The mechanical properties as well as the melting temperature of each of the three aluminum alloy sheets [22, 23] are given in Table 1.

Table 1 – Mechanical properties of the aluminum alloy sheets at the initial state before FSW joining

Aluminum alloy	**Melting temperature [°C]**	**Tensile strength R_m [MPa]**	**Yield strength at 0,2 % plastic deformation $R_{p0.2}$ [MPa]**	**Elongation at break A_t [%]**
AA 6061	585	120	65	22
AA7075	635	590	524	12
AA2024	500	465	340	17

The chemical composition and the density of each aluminum alloy sheet [22] are provided in Table 2. The welding tool (pin) that was used to assemble the three alloy sheets (see Figure 1) is made from highly alloyed steel, as required by the DIN 1.2312 standard for tools that are categorized P20+S (40 CrMnMoS 8-6). The pin is an M6-thread and its length of 5.3 mm covers 85% of the specimen thickness to be welded.

Table 2 - Chemical composition and density of each aluminum alloy sheet

Aluminum alloy	**Chemical composition (in percent by weight)**									Density (kg/m^3)
	Si	Fe	Cu	Mn	Mg	Cr	Zn	Ti	Ti+Zr	
AA6061	0,74	0.40	0.22	0.14	0,90	0.18	0.09	0.05	-	**2700**
AA7075	0.05	0.10	1.60	0.05	2.70	0.19	5,80	0.05	0.06	**2810**
AA2024	0.10	0.11	4,40	0.47	1.50	0.01	0.14	0.04	0.05	**2773**

The tool shoulder diameter of 22 mm sheets (see Figure 1) was sufficient to generate the required heat for assembling the three sheets together by using an FSW machine (4-10 model). This machine allows selecting the rotational speeds v_r, within the range of 300 to 1450 rpm, and advancing speed v_a from 10 to 480 mm/min. This machine also allows monitoring the plunging depth of the pin along the z-direction (Figure 1) while recording the corresponding force value all along the welding process. The temperature was measured using an infrared camera (FLIR A40M featuring a temperature resolution of +/-2°C) at the interface between the tool and the plates being welded (precisely 1 mm behind the tool and pointing to the weld bead). The kinematics parameters used in this study are as follows: $v_r = 1400$ rpm et $v_a = 70$ mm/min.

2.2 X-Ray Tomography

Computed microtomography (µCT) is an imaging technique that helps to have an overview of the internal structure of a test specimen without causing any damage. The non-destructive ability of this technique is a significant advantage in material science, particularly when performing in situ acquisition, as successfully experienced by Buffière et al. [24]. Moreover, this inspection technique is by far more efficient than numerous imaging methods such as microscopy-based ones since it provides 3D data with a resolution of up to 1 µm [24] and even lower, depending on the X-ray source used in the tomography equipment [25]. The X-ray computed tomography equipment (model Phoenix vTomeX / X-ray, see Figure 2) that was used during this experimental study is located in the MATEIS laboratory (INSA de Lyon, France).

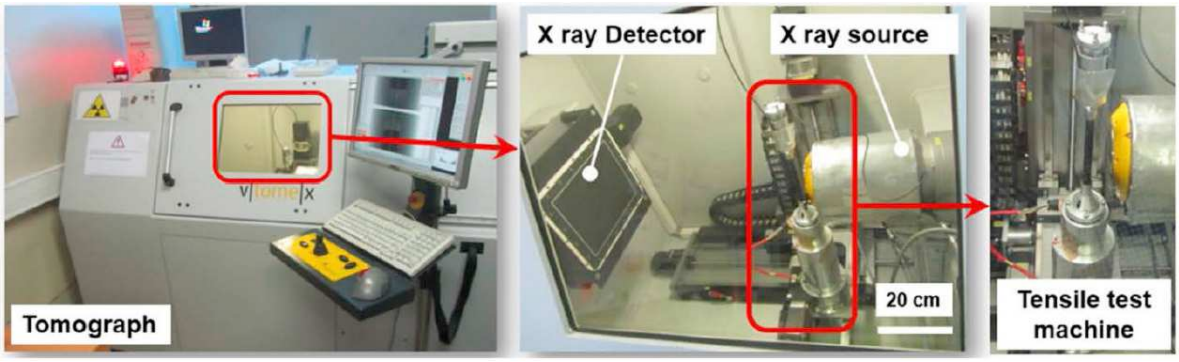

Figure 2 - X-ray computed tomography equipment, model Phoenix vTomeX (MATEIS/ INSA de Lyon)

The analysis of the FSW specimen required the use of incident X-rays that were characterized by a voltage of 80 kV and an intensity of 280µA without any filtering. The voltage of 80 kV was chosen to obtain the best compromise between transmission and contrast. Concerning the current, the maximum value (before defocusing) was used to obtain the maximum photon flux without increasing the source spot size.

Under these conditions, the source spot size was about 2-3 µm. The Varian Paxscan X-ray detector used in this study has an active surface of 200 mm x 250 mm along with a matrix of 1920×1536 pixels^2. This detector records radiograms that are encoded in greyscale, with a gray depth equal to 14 bits. The size of the reconstructed volume is 1500 x 1000 x 500 voxels^3 and the size of a voxel after reconstruction is equal to 18 x 18 x 18 µm^3. The data acquisition was performed by using the following procedure: 912 projections of X-rays were considered during the 360-degree rotation of the specimen and the exposure time for each angular position was equal to 333 ms. The resulting 3D images were reconstructed by using a filtered back-projection algorithm [26] which is implemented in the software provided with the tomograph. Information on the theory and the techniques used to reconstruct 3D images can be found in [27].

2.3 Localized Spectrum Analysis

The purpose here is to measure the strain fields that occur on both the front and the lateral faces of the specimen and to observe whether some coupling exists between the pattern of these strain fields and the internal structure of the solder characterized by tomography, or between these patterns and AE events. The constitutive material being strongly heterogeneous in this zone, strain fields are also expected to be heterogeneous. The technique to be used should therefore ideally be able to distinguish close features in the strain maps, and these maps should be as little as possible impacted by noise and systematic errors. Digital Image Correlation is the most popular full-field measurement technique [28]. It consists of retrieving displacement and strain fields from images of speckled surfaces taken before and after deformation. However, it has been recently shown in [29] that considering periodic patterns like checkerboards instead of random speckles, and processing the corresponding images with a suitable spectral technique named Localized Spectrum Analysis (LSA) led to much better metrological performance, especially in terms of noise level, ability to distinguish close features in strain maps and systematic errors. The present specimen was therefore marked with such checkerboard patterns by using the transfer technique described in [30]. The period

of the checkerboard was 0.1 mm, and the size of the squares forming the checkerboard was 50 microns. Figure 3 shows a close-up view of such a pattern. It can be seen that the natural symmetry axes of the checkerboard are inclined by an angle of 10 degrees with respect to the borders of the image. This enables us to avoid the presence of possible parasitic fringes in the strain maps due to aliasing, as explained in [31] in the case of periodic grid patterns. The LSA technique as described in [32] was finally used to process the checkerboard images to extract the displacement and strain fields.

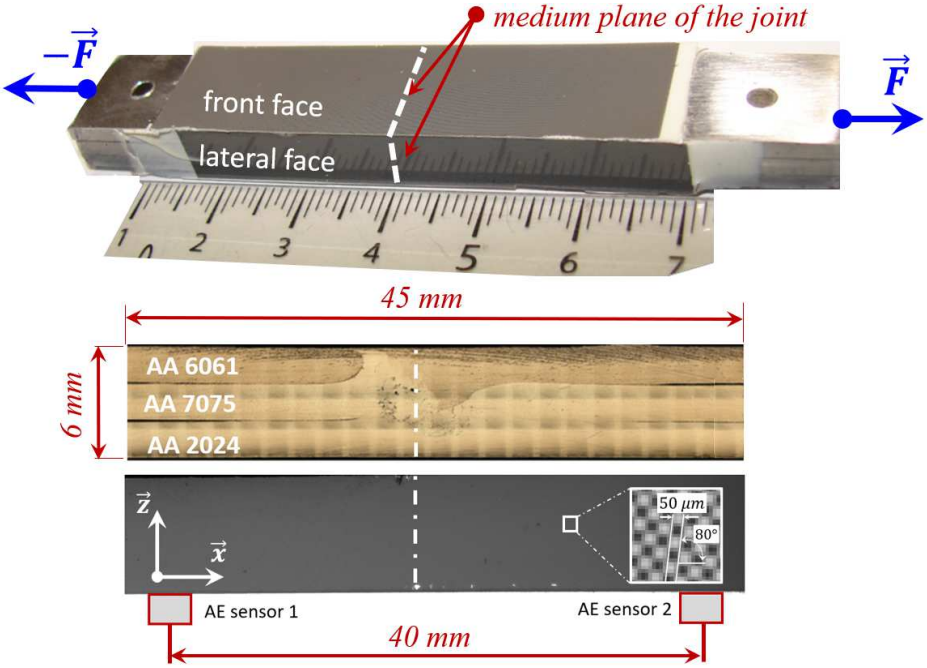

Figure 3 - LSA checkerboard patterns and AE sensors

2.4 Acoustic Emission (AE) monitoring

The purpose of AE monitoring is to analyze the mechanical vibrations emitted by the specimen after a sudden modification of the internal structure of the welded joint during the test. These vibrations can be due to damage, cracking, or plastic deformation for instance. Thus, under mechanical loading, the rapid release of energy from localized cracks within the welded joint generates transient elastic waves, referred to in this paper as AE waveforms. The latter propagate from the crack throughout the specimen before being detected by AE sensors. Thus, in addition to the displacement field measurement, a four-channel AE system equipped with Physical Acoustics' PCI-8 AE boards and pre-amplifiers was used to record the AE waveforms during the test. Due to the small dimensions of the specimen (see Figure 1), two lightweight miniature piezoelectric sensors with an optimum operating frequency range of

200–750 kHz were bonded on the specimen with a double-face adhesive tape. They were used to perform a linear localization of AE sources (also termed AE events). The propagation velocity of AE waveforms was set at 4000 m/s following the pencil lead-breaking tests. The AE signal acquisition threshold was set at 50 dB, which is slightly above the surrounding noise.

2.5 Tensile test set-up

The main dimensions of the specimen subjected to monotonic tensile loading are reported in Figure 1. An INSTRON servo-hydraulic testing machine (model 1342) equipped with a +/- 100 kN cell force was used to perform the tensile tests at a controlled crosshead speed of 0.5 mm/min.

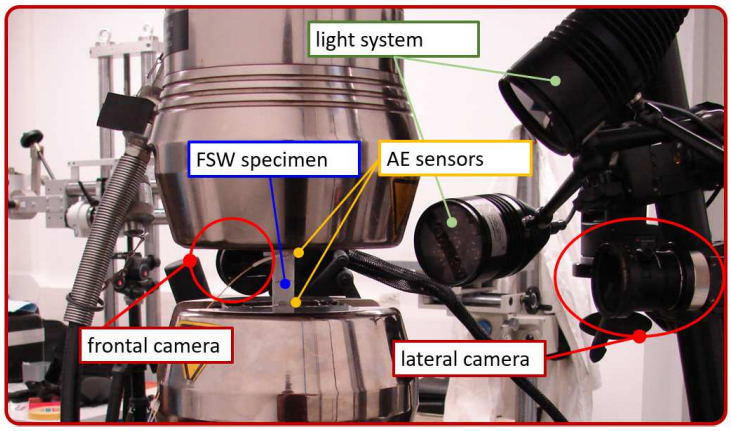

Figure 4 - General overview of the laboratory experimental setup

The displacement and strain fields occurring on two perpendicular faces of the FSW specimen (the front and the lateral ones) were measured by simultaneously using two cameras (Aramis-GOM system), as shown in Figure 4. Their CCD sensor size is 2448 x 2050 pixels^2. The two cameras were synchronized with each other and with the INSTRON testing machine. Hence the tensile force corresponding to every couple of images was recorded. The checkerboard patterns were transferred to both the front and the lateral faces. These latter are represented in Figure 1 as the IJKL and LKMN rectangles that are centered over the welded joint. Their length was equal to 40 mm to allow recording the images of the whole faces until specimen failure. A polarized lighting device was also set up for recording images with high contrast at a frequency of 1 Hz. The mechanical loading was applied along the x-direction (Figure 1), which corresponds to the longitudinal direction of the specimen. For strain analysis, the spatial resolution was equal to 36 pixels with a standard deviation of about 200 $\mu\varepsilon$.

The AE sensors were placed on the specimen, symmetrically on both sides of the welded joint. They were spaced 40 mm apart. The monitoring of AE activity from the specimen was synchronized with both the image acquisition system and the testing machine.

3. Results and discussions

3.1 Thresholding and segmentation

The specimen volume investigated by using X-ray computed microtomography is shown in Figure 1. It is represented by the blue parallelepiped (ABCDEFGH) centered over the median plane (see dotted lines) of the welded joint. The size of this volume was chosen to identify relatively small size defects (voxel size in reconstruction = 18µm) but also the morphology of the melted alloys mixture. As mentioned in Section "2.2 X-Ray Tomography" above, the initial state of the internal structure of the specimen has been analyzed using the ImageJ software [33]. This is an open-source software dedicated to image processing and analysis. It can be extended with plugins and macros. The data processing steps described below were applied to the reconstructed volume. First, the quality of this latter was improved through the use of a 3D median filter of size 3 x 3 x 3 voxels^3. This allows reducing the noise level that could affect the different steps of both the thresholding and segmentation steps. Then, to analyze the whole volume and not be dependent on the random-access memory, the encoding of the volume was reduced from 14 to 8 bits. Loss of information following this re-encoding had almost no effect on the qualities of detected phases. To illustrate this, Figure 5-a shows five sections that are parallel to the FEHG face (Figure 1) for different values of y. The average gray level for a 8 bit gray depth is 99.5, 136.1, and 120.7, for the AA6061, AA7075, and AA2024 alloys, respectively. This difference is in good agreement with the density variation of each alloy, as shown in Table 2. Indeed, the density is slightly different for each alloy being welded. This is a great advantage to fully understand the mixing of these three materials.

For efficient analysis of data from the studied volume, it is necessary to perform segmentation to separate the different phases: the air surrounding the specimen, the pores, or the spatial distribution of the different welded aluminum alloys. The simplest way to segment data into polyphasic grey levels consists of using thresholds [34, 35]. The latter can be manually selected or preferably computed algorithmically. Because of the form of the volume histogram, a so-called Otsu threshold [36] was applied. In his paper, Otsu demonstrates that a threshold can be computed to segment bimodal data by maximizing the inter-class variance of

the grey levels in each class. Yet, it is necessary to generalize this approach to some thresholds greater than one. The idea here is not to separate each alloy sheet, even if the reconstructed data allow it, but also and particularly to automatically block out the air surrounding the specimen before identifying the porosity. Both components were detected by using the same thresholding level. In this case, the differentiation between the air surrounding the specimen and the porosities generated during the FSW process lies in the volume of the characteristic size associated with each phase as it is quite obvious that the air surrounding the specimen is characterized by a volume greater than that of the biggest identified porosity. Then, the thresholding step (grayscale level lower than 30) was applied again over the specimen volume without its surrounding air to separate the pore-type defects within the join. The pores distribution is shown in Figure 5-b. All pores having a size lower or equal to that of the 3D median filter (pores with sizes lower than 60 µm) are not considered representative, the noise effect on their detection being too high. One can also notice by superimposing the pin over the different cross-sections shown in Figure 5-a that the highest volume fraction of pores is located on the advancing side at the edge of the pin, and at the interface between the AA7075 and AA2024 aluminum alloy sheets.

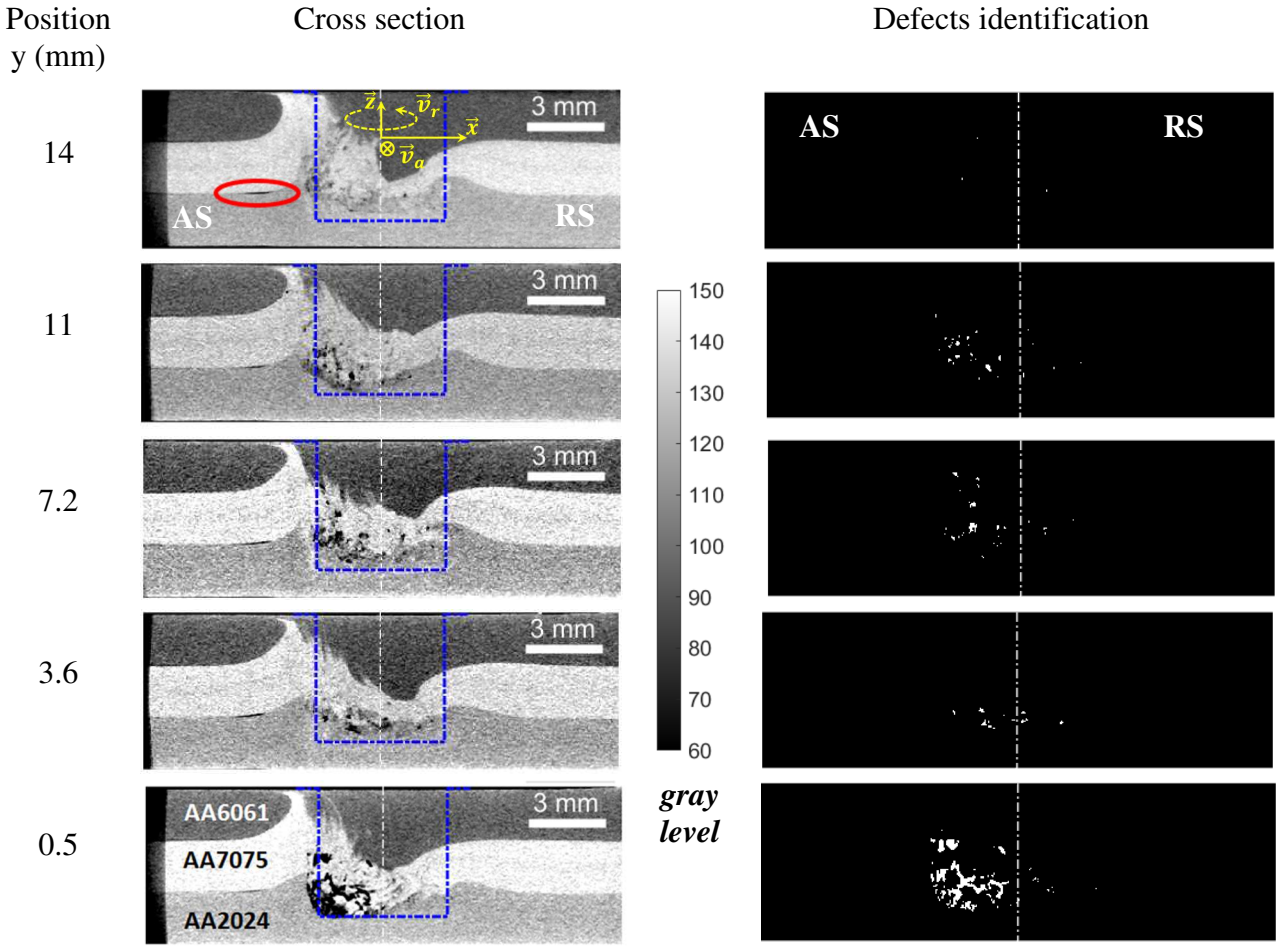

a) - several cross-sections from the reconstructed volume. The welding tool geometry is superimposed over each picture and represented by the blue dotted line.

b) - porosities detected within several cross-sections

Figure 5 - Reconstructed data after filtering and pores identification

3.2 Defects measurement by X-Ray µtomography

3.2.1 Distribution of the pores in the joint

Computed microtomography is a highly efficient tool for the analysis of a structure consisting of several phases characterized by various densities [37]. This experimental technique provides relevant details on the investigated welded joint, as shown in Figure 5. These pictures allow an in-depth understanding of the effects of the welding parameters on joint quality. It helps predict different failure mechanisms (initiation and propagation of cracks) which occur when the joint is subjected to mechanical loading. First, one can observe the spatial distribution of the three alloys in the vicinity of the pin. This visualization was made possible because of the difference in the density values of the tested alloys (see Table 2). One can see that the AA6061 and AA7075 alloys are well mixed. Few pore-type defects are visible at the interface between the two alloys. These defects are located in the welding direction. In Figure 5-a (at y = 14 mm), hooking defects are also observed. This leads to a lift of the interface between two sheets. These hooking defects are generated by the translation of the material in its pasty state. This translmation is caused by the threaded welding tool. The formation of the hooks as well as their contribution to the mechanical behavior of the welded joints have been studied in [14] for instance. Different hook sizes and shapes were observed in this reference. These features depend on the welding parameters (welding speed, rotational speed, and advancing speed). By coupling digital image correlation (DIC) and tomographic analysis during tensile-shear tests, it was found that the hook characteristics govern the fracture behaviors and, consequently, the mechanical properties of the whole welded joints.

We focus here mainly on the characterization of the pores and their distribution within the joint. The spatial distribution of the detected pores is visualized in three dimensions (Figure 6-d). The porosity is evaluated along each of the three directions of the specimen volume in order to identify the areas that are highly affected by the defects. The formula used to calculate these porosity values are as follows:

$$X\ porosity\ (x) = \frac{S_{pores}(x)}{S_{0x}} \times 100 \quad \text{(Eq.1)}$$

$$Y\ porosity\ (y) = \frac{S_{pores}(y)}{S_{0y}} \times 100 \quad \text{(Eq.2)}$$

$$Z\ porosity\ (z) = \frac{S_{pores}(z)}{S_{0z}} \times 100 \quad \text{(Eq.3)}$$

Where S_{0x} is the FBCG cross-section (see Figure 1) along the $\vec{x}$-direction and between points G and H within the reconstructed volume. The cross-section is considered as constant over the calibrated area of the specimen. S_{0y} represents the FEGH cross-section (see Figure 1) along the $\vec{y}$-direction and over the whole width of the specimen. S_{0z} is the ABFE cross-section (see Figure 1) along the $\vec{z}$-direction and over the thickness of the specimen. $S_{pores}(x)$ represents the cross-section of the pores. It is perpendicular to the $\vec{x}$ axis and computed between points G and H, within the reconstructed volume. $S_{pores}(y)$ is the cross-section of the pores on areas that are parallel to FEHG (see Figure 1) along the $\vec{y}$-direction. $S_{pores}(z)$ represents the cross-section of the pores on zones which are parallel to ABFE along the $\vec{z}$-direction (see Figure 1). Figure 6-a shows the evolution of $X\ porosity\ (x)$. Monitoring this porosity provides some information that are useful for understanding the evolution of the real cross-section of the joint. First, one can note that the pores are mainly located along a segment that is nearly centered (+/-3 mm) around the location of the welding tool axis along a zone, which is greater than the pin diameter. The zone, which is the most affected by the pores is located within the advancing side and at -3 mm from the pin axis. At this position, the cross-section of the specimen is reduced by slightly more than 2.5%. This is likely the zone where the very first cracks would be initiated. One can also point out a rapid and gradual decrease in the number of pores towards point E since the value of the cross-section at this position is nominal. Figure 6-b shows the evolution of $Y\ porosity\ (y)$. This characterizes the distribution evolution of the pores along the specimen width, in other words in the welding direction. Based on the analysis of this evolution, one can conclude that the welding process is locally not completely stabilized. This is probably due to a discontinuous interfacial contact during the welding phase and to the fact that the fusion temperature of the AA7075 alloy is higher than those of the AA6061 and AA2024 alloys. It is worth noting that this evolution should lead to heterogeneous stress distribution during a tensile test. Consequently, the strain distribution should also be heterogeneous over the whole width of the specimen. Finally, the pore

distribution along the $\vec{z}$-direction is analyzed through the parameter $Z\ porosity\ (z)$. This quantity is plotted in Figure 6-c. 60% of the specimen width is affected by the pores, with a high concentration at the interface between the AA7075 and AA2024 alloys. This zone featuring high pore concentration is located at about 4 mm below the contact surface between the pin shoulder and the AA6061alloy sheet. This is, firstly, because the heat, which is generated mainly from friction between the pin shoulder and the AA6061alloy sheet, is not continuously spread out due to some discontinuities such as the thin air layers, which are visible in Figure 5-a. They appear between the alloy sheets to be welded and in the vicinity of the pin, and as a consequence the appearance of a strong temperature gradient in the joint thickness and a reduction in the effective welding temperature of the AA7075 and AA2024 sheets. A significant difference between the effective welding temperature and the optimal one (supposed to be equal to [0.7 to 0.8] times T_f(°C) [38], this latter being the melting temperature) can result in pores appearance. The volume fraction of these pores is proportional to the difference between the effective welding temperature and the optimal one.

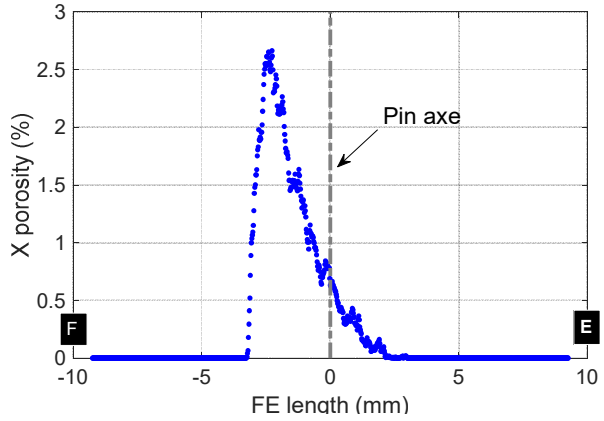

a) defects distribution along the $\vec{x}$-direction

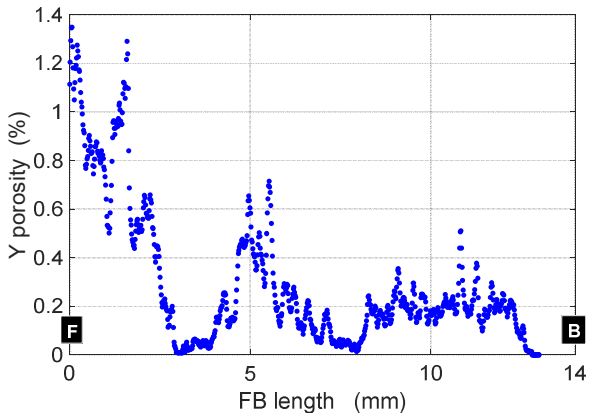

b) defects distribution along the $\vec{y}$-direction

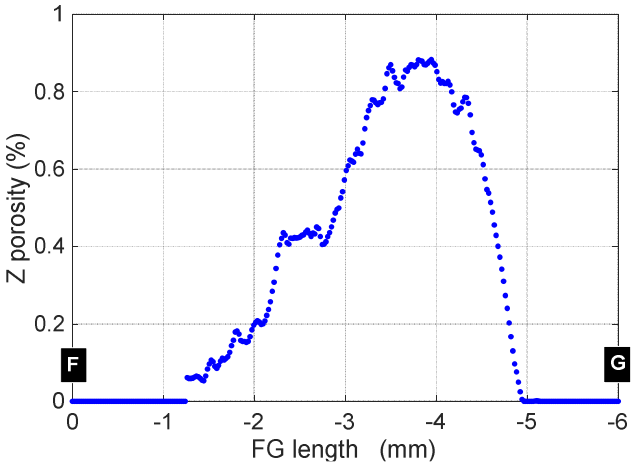

c) defects distribution along the $\vec{z}$-direction

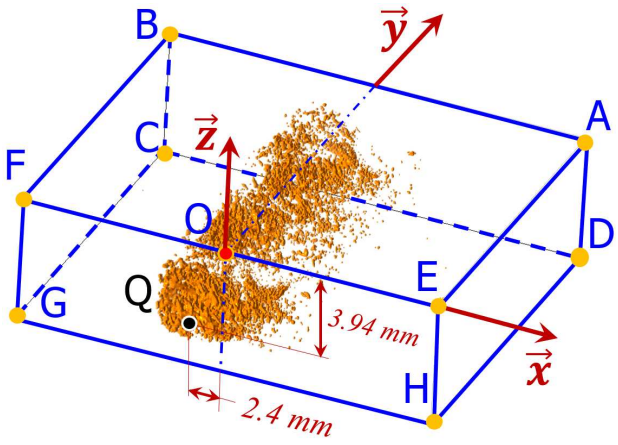

d) 3D view of defects distribution

Figure 6 - Internal defects distribution within the welded joint

Given the foregoing, it can be argued that the zone where the fraction of pores is maximal is represented by point "Q" in Figure 6-d. The coordinates of this point are the following: x = -2.4 mm, y = 0 mm, and z = 3.94 mm.

3.2.2 Local porosity fraction

Similar strategies can be applied to identify in the $\vec{x}O\vec{z}$ plane and along the $\vec{y}$-direction (see Figure 1) the zones that are characterized by a high volume fraction of pores. To this end, a similar approach has been applied thus allowing to calculate the compacity parameter η_{loc}, defined in Equation 4. This parameter, referred to as the local porosity volume fraction, takes the form of either a matrix $M_{pores} = [m, p]$ for the segmented pore phase or a Boolean matrix $M_{joint} = [m, n, p]$ for the whole joint. These matrices are computed as follows:

$$\eta_{loc}(i,k) = \frac{\sum_{j=1}^{n} M_{pores}(i,j,k)}{\sum_{j=1}^{n} M_{joint}(i,j,k)} \times 100 \qquad \text{(Eq.4)}$$

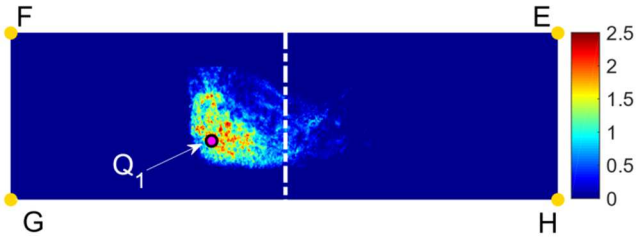

Figure 7 - Compacity of the joint in the $\vec{y}$-direction

The map, shown in Figure 7, allows one to point out that the zone which exhibits the highest pore volume fraction is located within the AA7075 alloy sheet and on the advancing side. In this area, the maximal value of η_{loc} is 2.5% (shown by point Q_1in Figure 7). There is a good agreement between the η_{loc} map and the details observed on the lateral face of the specimen shown in Figure 3. However, the most affected zone, in other words, the one characterized by a value of η_{loc} greater than 1.5%, is mainly located within the AA7075 alloy sheet and along the whole width of the specimen ($\vec{y}$-direction).

3.2.3 Equivalent diameter, maximal length of the major axes, and shape of defects

Another method could be used to analyze the defect distribution within the joint. It consists of evaluating both the size and the center of gravity of each defect along the welding line. The distribution of the diameter of 4275 pores is plotted in Figure 8. Once again, only the pores

having a diameter greater than 60 µm are considered in this histogram. Significant fluctuations of the equivalent diameter of the defects can be observed. This diameter lies between 0.06 mm and 1.2 mm, with a high concentration between 0.06 and 0.3 mm.

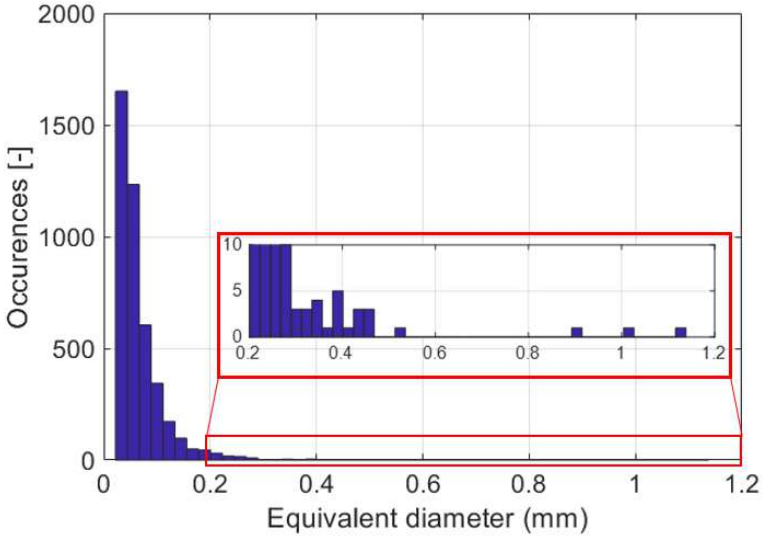

Figure 8 - Number of defects as a function of their equivalent diameter

The equivalent diameter is well suited to characterize spherical-shaped defects. Thus, one can see in the present study (see Figure 5) that the shape of larger defects is far different from a sphere. To better understand the defect distribution within the joint and to have a more realistic picture of the effective size of the defect, we focused on the longest major axis of the defect. This axis represents the major axis of the ellipsoid that has the same normalized second central moments as the defects under investigation [39].

Figure 9-b shows the spatial distribution of the defects as a function of their center of gravity as well as the size (color level) of the longest major axis. It should be noted that the defects under 0.5 mm in size are asymmetrically distributed (78% of them are located on the advancing side) with respect to the welding line. It is very clear from Figure 9-a that the defects characterized by a maximal length of the major axes greater than 1 mm are all located on the advancing side, with a downward trend for positive values along the y-axis. It should also be noted that the defects are spread out over three main zones that are defined by their position along the y-axis. This result is in very good agreement with the Y porosity evolution shown in Figure 6-b.

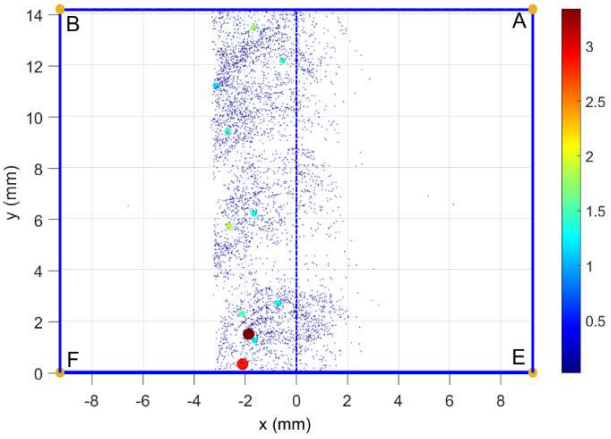

a) Size and centroid of the defects distribution projected in the XY plane (front view)

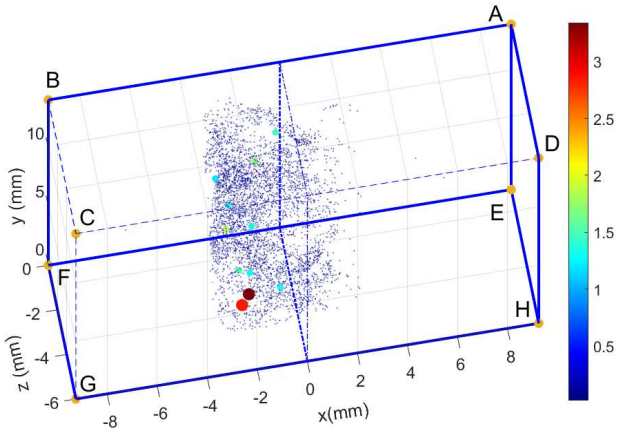

b) 3D view of the size and centroid of defects distribution

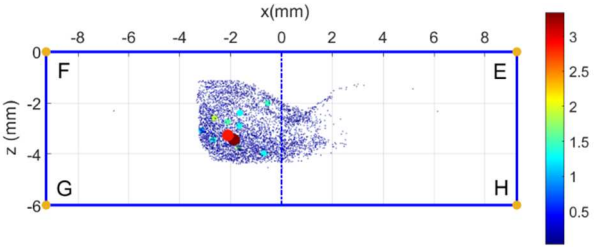

c) Size and centroid of the defects distribution projected in the XZ plane (lateral view)

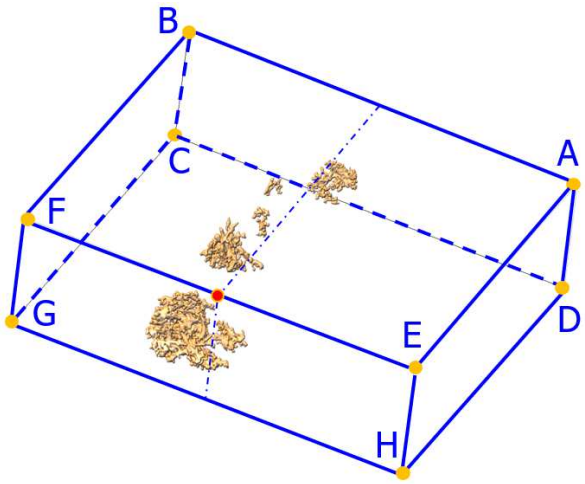

d) 3D defects distribution of the six largest defects

Figure 9 - Centroid, maximal length of the major axes, and shape of defects. The color scale represents the size (the major axes) of defects in mm.

Figure 9-c shows that these defects are mainly located within the melted area of the three alloys. A high density of defects was also observed in the initial position of the AA7075 alloy sheet. As a complement to the above analysis, we plotted the six largest defects in Figure 9-d. In this figure, it is clear that the shape of the defects is complex since it looks like a network of interconnected defects, as previously observed in [11]. It's worth noting that the largest defect is characterized by a maximal half-axis of length 3 mm. It is located close to the EFGH plane. These complex shapes that spread out over a few millimeters should probably negatively affect the strength of the assembly because they should be activated first when the joint is subjected to mechanical loading.

3.2.4 Sphericity of the defects

As a complement to the above analysis, the shape of defects has been thoroughly characterized by computing its sphericity denoted by ψ. The latter represents the similarity level between the shape of an object and a sphere. The rate of sphericity ranges between 0 and 1. For example, it equals 1 for a sphere, 0.806 for a cube, 0.874 for a cylinder, and 0.671 for a tetrahedron.

The formula used to compute the sphericity is the one proposed by Wadell in 1935 [40]. It is given in Equation 5. In this formula, V_p and A_p represent respectively the volume and the surface of the defect.

$$\psi = \frac{\pi^{\frac{1}{3}}(6V_p)^{\frac{2}{3}}}{A_p} \quad \text{(Eq.5)}$$

The evolution of the sphericity as a function of the equivalent diameter is plotted in Figure 10-a. It can be seen that most of the defects, particularly those under 0.1 mm in diameter, exhibit a shape close to a sphere whereas the largest defects are characterized by sphericity slightly lower than 0.2, which means highly complex shapes. To illustrate this, we superimposed on the same figure the shape (not to scale) of different types of defects that are characterized by sphericity of 0.96, 0.45, and 0.16. One can also see from this figure that for some defects, the sphericity is greater than the theoretical limit of 1, particularly for those with the smallest equivalent diameters. This can be due to the voxelization effect during data acquisition since the size of the voxel is 18 µm. For very small objects, this can lead to aberrant rates of sphericity because of miscalculations of the volume [40].

It is also interesting to plot the sphericity as a function of the initial position of each defect. This position is represented by the coordinates of the center of gravity. Figure 10-b shows the spatial distribution of the defects. The color scale is correlated with the rate of sphericity. The red dots have a rate of sphericity close to one while the blue ones indicate a value close to zero. It is clear that defects with a low rate of sphericity, in other words, characterized by a high equivalent diameter, are located on the advancing side of the joint. Based on another graphical presentation (Figure 10-d) it can be seen that the defects characterized by a sphericity lower than 0.4 are spread out over three main zones. The first one located between y = 0 and y = 4 is the most affected (presence of 8 defects characterized by an equivalent diameter greater than 0.4). This leads to a weakening of the strength of the joint because its effective cross-section is reduced in this zone. The appearance of these zones is undoubtedly due to the inhomogeneity of the mixing during the welding process associated with a local change in both the welding temperature and the force applied by the welding tool.

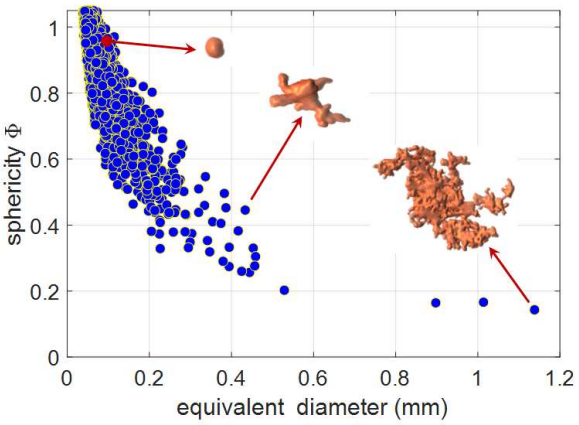

a) the sphericity as a function of the equivalent diameter

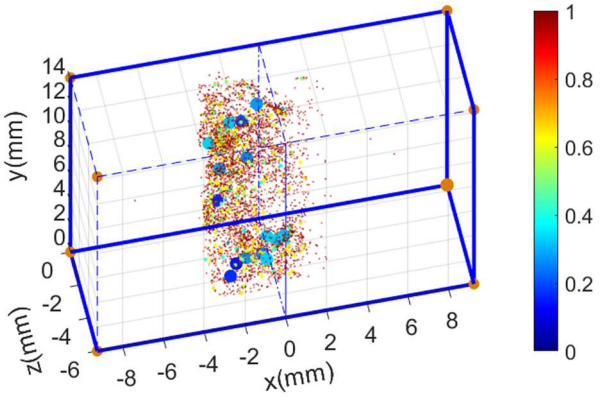

b) 3D view of the sphericity distribution

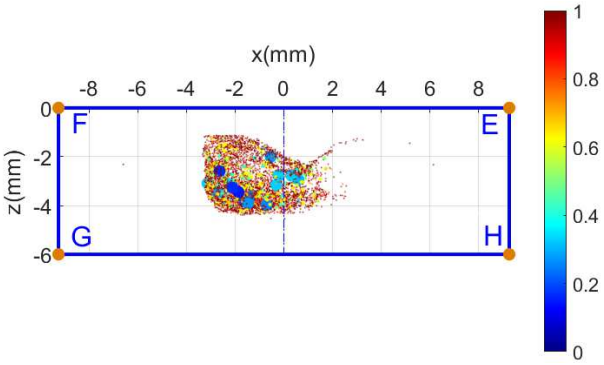

c) sphericity distribution projected in the XZ plane (lateral view)

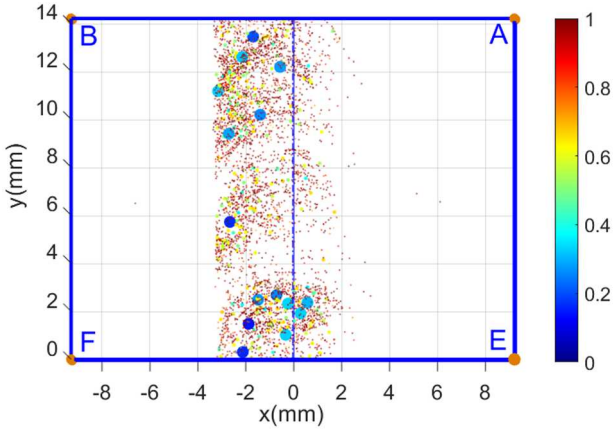

d) sphericity distribution projected in the XY plane (front view)

Figure 10 - Defects distribution as a function of their sphericity. The color scale represents the sphericity of defects.

Figure 10-c shows the distribution of defects over the thickness of the joint. It should be noted that the most irregular defects, which are characterized by a complex shape, are located in the AA7075 alloy sheet and at the interface between this sheet and the other two alloy sheets.

3.3 Macroscopic and local behavior

The macroscopic mechanical behavior (nominal stress $\bar{\sigma}(MPa)$ versus nominal strain $\bar{\varepsilon}(\%)$) of the three alloy sheets subjected each to monotonic tensile loading is shown in Figure 11. A loading rate of 1 mm/min (crosshead speed) was applied in each case. Three tests were carried out with a very good repeatability in terms of elongation and maximum stress at failure. For each configuration, good reproducibility of the tensile tests is observed. However, only one curve by tested configuration has been plotted for the sake of clarity. These results show that

the welded configuration leads to a tensile strength lower than those of the other specimens except the AA6061 alloy sheet. The presence of a significant density of defects within the joint is undoubtedly the cause of the early cracking of the assembly and thus the low strength of the weld. This strength is 37% lower than that of the non-welded configuration obtained by only superimposing the three aluminum alloy sheets. As a consequence, the macroscopic nominal strain at specimen failure is equal to 1.4%, which is also low compared to its counterpart obtained with a specimen made up of three superimposed but non-welded alloy sheets. The latter configuration leads to a nominal strain at failure of about 7.75%, see Figure 11.

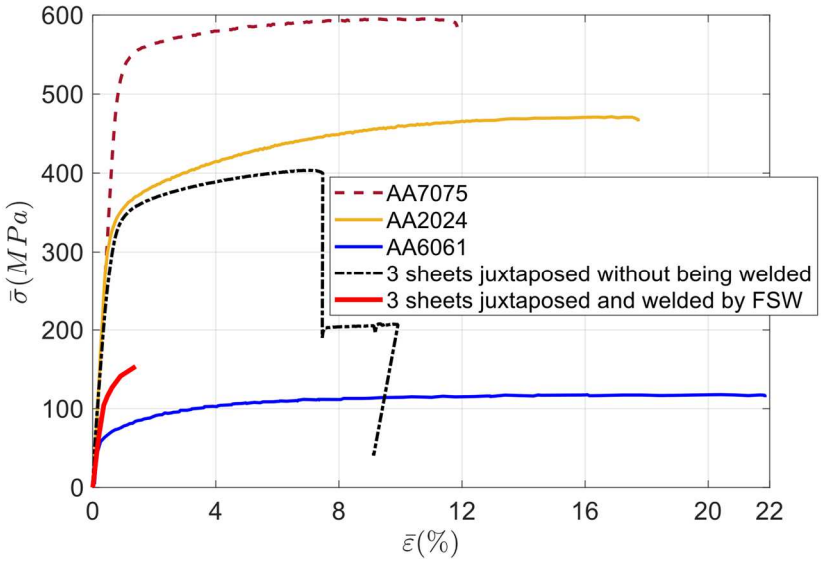

Figure 11 - Macroscopic mechanical behaviors of a specimen made of the studied alloy sheets, a specimen made of non-welded superimposed alloy sheets, and the FSW specimen under study.

Based on the microtomographic analysis presented above, one can state that this FSW welding configuration is characterized by a very heterogeneous defect distribution. This distribution leads to the appearance of stress concentrations which are added to the residual stresses resulting from the welding process. To better understand the effect of the defects on the joint behavior, we investigated the strain local fields along the loading direction. Figure 12 shows the macroscopic strain of the FSW specimen. The nine black dots represent the moments at which the strain field (ε_{xx}) evolution was finely analyzed along the loading direction, on the front and lateral faces (IJKL and LKMN, respectively), see Figure 1. The

first four dots, labeled a, b, c, and d, lie in the quasi-linear elastic portion of the macroscopic response whereas the last five, labeled e, f, g, h, and i, are located in the non-linear portion of the response.

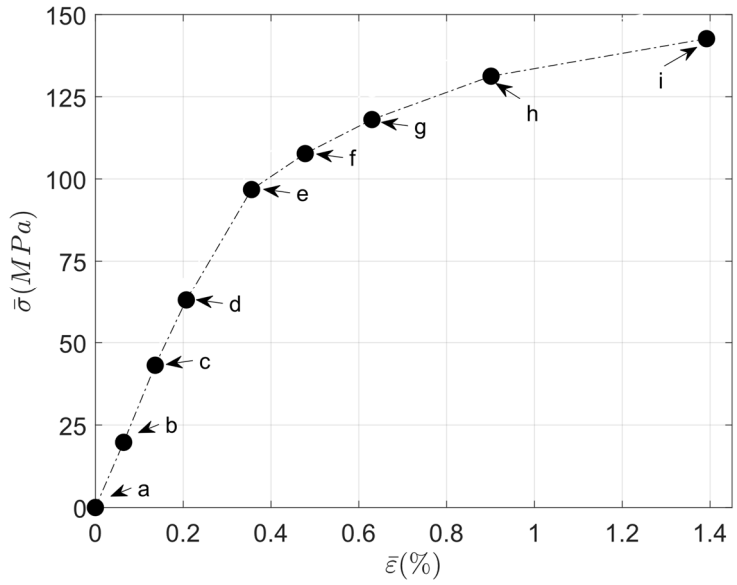

Figure 12 - macroscopic behavior of the FSW specimen

Figure 13 shows with a good spatial resolution the strain field (ε_{xx}) measured on the front face of the joint. Thanks to the LSA technique that is powerful to get small strains values over small regions, it can be seen that small strain peaks are detected early (dot labeled b), namely for macroscopic stress levels lower than 20 MPa. These strain peaks are located at the interface between the AA7075 and AA2024 alloy sheets and on the advancing side. There is a very good agreement between the deformed zone and the one characterized by a high density of defects, as identified from the microtomography results analysis. In addition, the location of the deformed zone is very close to that of the point Q represented in Figure 6-d above. It should be noted that this deformed area is progressively widening when the nominal stress reaches the values represented by the dots c and d (Figure 12), leading to an increase in the local deformation of nearly 2% for a corresponding macroscopic strain ten times lower. The transition between the elastic-linear portion and the non-linear one, which is materialized by the dot labeled e, highlights a significant growth of the value of the local strain field, which clearly means a crack initiation. This crack propagates when the stress level reaches that of dots f, g, and h, successively. The crack propagation path is easily visible from the strain

maps (see Figure 13). The form of the crack path shown on these maps only makes sense for the lateral face of the specimen under investigation. This crack path may have a three-dimensional shape within the volume of the welded joint but this is not detectable by this 2D strain measurement technique.

The strain field map associated with the testing moment labeled i (Figure 13) exhibits a crack bifurcation when the specimen fails, thus enabling monitoring of the crack propagation through each alloy sheet.

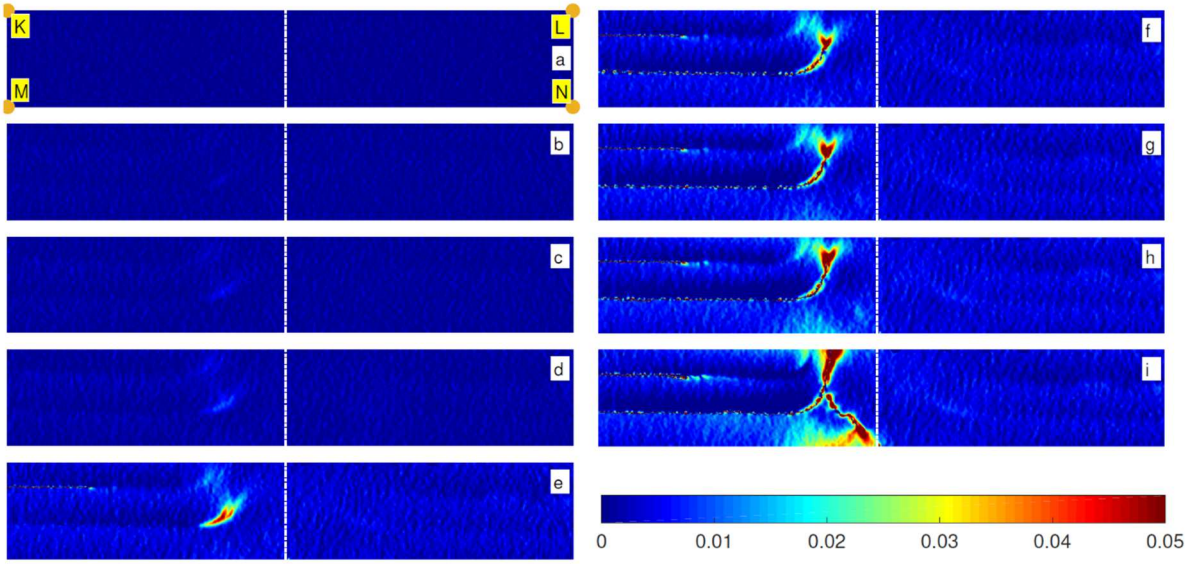

Figure 13 - Local strain field (ε_{xx} [in ***μdef***]) maps on the joint lateral face

The strain maps measured on the front face (see Figure 14) provide additional information. These maps computed at the first four testing moments (dots: a, b, c, and d) do not put in evidence notable deformation zones. Strain values observed on these maps are in good agreement with both the deformation measured on the front face (on the AA6061 alloy sheet) and the macroscopic nominal strain. Similarly, one can see on these maps a 2 mm-wide strip where the local strain value is close to zero. This strip is still visible in the non-linear portion of the macroscopic behavior (dots labeled e to i). It represents the area where the specimen, particularly the front face, fails. To understand why the strain value is low within this strip, it is necessary to correlate the strain maps with the different results obtained from the microtomography analysis and presented in Figure 5. One can see from this figure that the AA7075 alloy sheet moves and penetrates in the AA6061 alloy sheet. Figure 11 shows a significant difference in the yield strength values of the alloy sheets. This suggests that when the FSW specimen is subjected to mechanical loading, the AA6061 alloy sheet deforms,

which is not the case for the strip of AA7075. Moreover, the welded area, which is composed of an AA7075 portion melted with AA6061, exhibits a low strength. Indeed, this is where the crack initiates, as shown on the maps corresponding to points f, g, h, and i (Figure 14). One last analysis of the strain maps of the front face, particularly those labeled g, h, and i, highlights a localized deformation, which is much larger on the advancing side than on the retreating one.

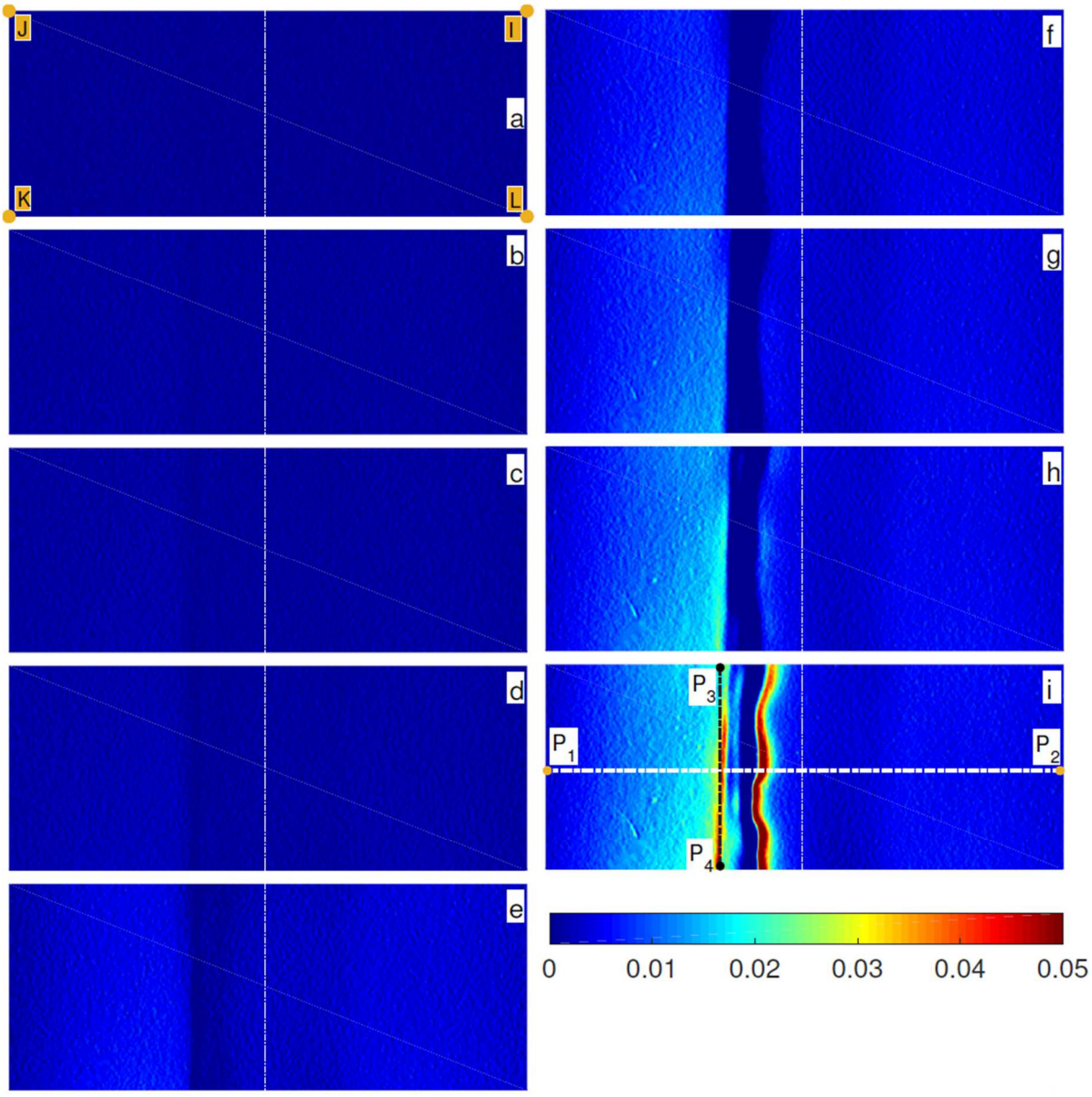

Figure 14 - Local strain field (ε_{xx} [in ***µdef***]) maps of the joint front face

To show a very representative evolution in the strain field measured on the front face, two cross-sections of the maps at points b, e, and i along the $\vec{x}$- and the $\vec{y}$-direction, labeled P_1P_2 and P_3P_4 respectively, are shown in Figure 15. First, Figure 15-a shows the strain field

evolutions along the $\vec{x}$-direction ($\mathrm{cross-section\ P_1\ between}\ P_2$) at different values of the time. The curve deduced from map b is fairly regular whereas the curves from maps e and i are more heterogeneous. Sharp strain peaks appear as the FSW specimen is close to failure. This graphical representation highlights once again the existence of a strip of AA7075. It corresponds to the portion of the strain fields measured along the loading direction and on the front face is close to zero. Figure 15-b puts in evidence the strain field evolution along the $\vec{y}$-direction (cross-section between P_3 and P_4). Even though the strain curve deduced from map b remains constant and small, one can see that the one from map i exhibits values ranging between 1.5% (in the vicinity of the point P_3) and 4.5% (in the vicinity of the point P_4). A linear trend is observed. This evolution along the $\vec{y}$-direction can be linked to that of the $Y\ porosity\ (y)$ curve shown in Figure 6-b. It can be seen from this figure that the value of the $Y\ porosity\ (y)$ is about 0.2% and 1.4% in the vicinity of the points P_3 and P_4, respectively. This evolution of $Y\ porosity\ (y)$ could locally reduce the effective cross-section of the specimen, thus leading an important part of the tensile loading to be transferred through the AA6061 and AA2024 alloy sheets. This is especially true in the vicinity of the point P_4. These results show once again how it is complex and difficult to investigate this type of welding configuration by using classic measurement tools and standard approaches.

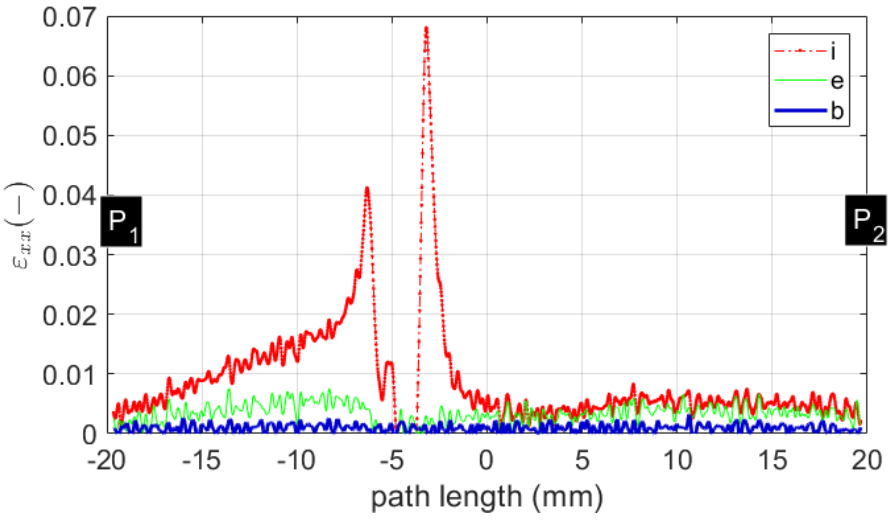

a) ε_{xx} of the front face: mean values projected along the $\vec{x}$-direction

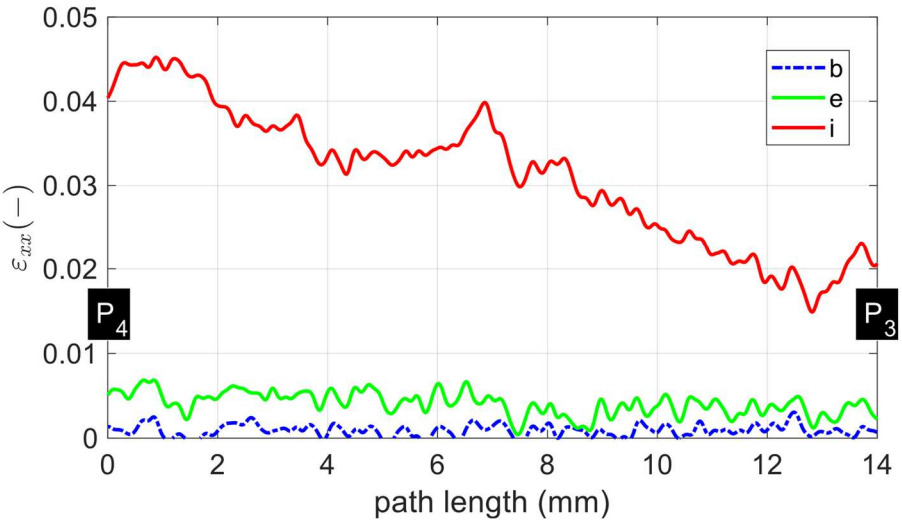

b) ε_{xx} of the front face: mean values projected along the $\vec{y}$-direction

Figure 15 - Mean values of ε_{xx} projected along two directions

3.4 Acoustic Emission activity

The AE activity during the tensile test is first analyzed by focusing on the localization of AE events within the FSW joint (Figure 16). The results show that cracking starts in the lower half of the joint before spreading throughout the assembly. The very first AE events appear for a stress value equal to 73 MPa.

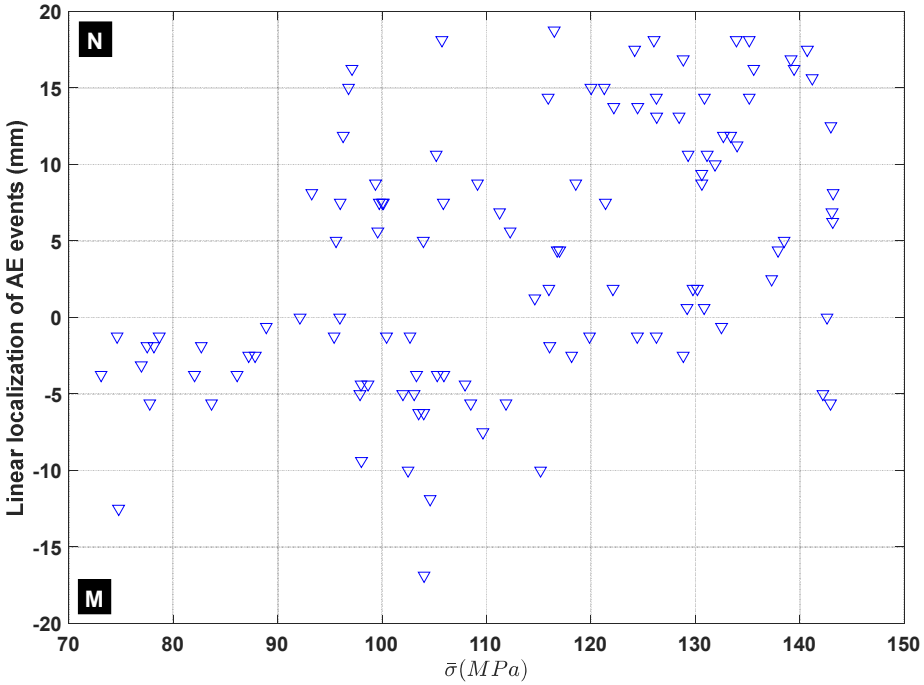

a) Linear localization of AE events as a function of the applied macroscopic tensile stress

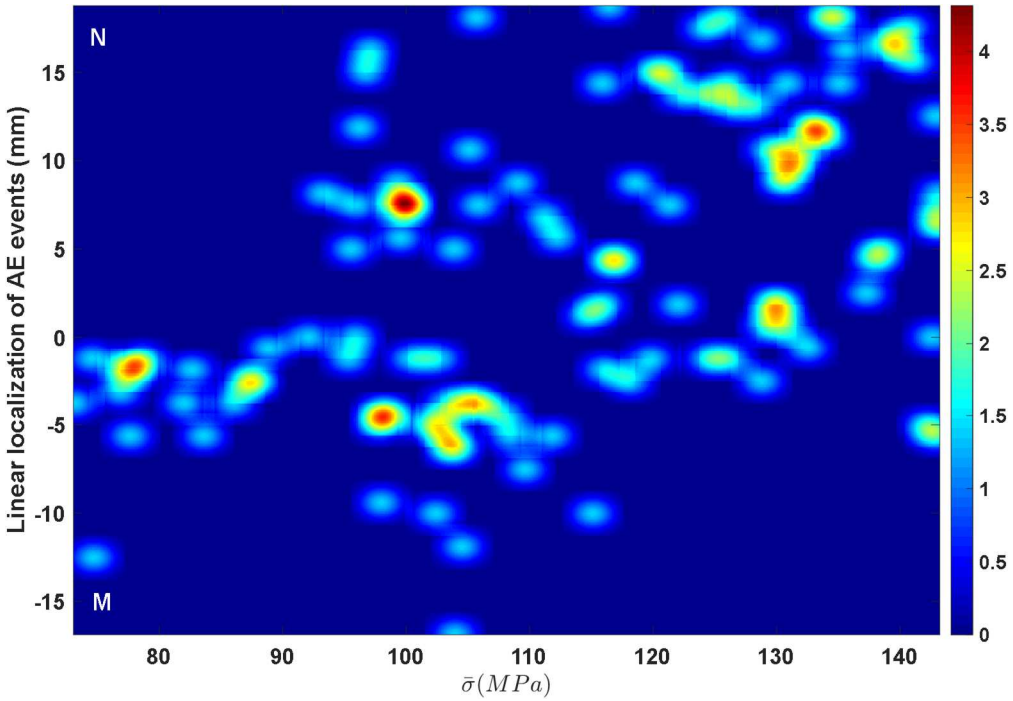

b) Map of AE events concentration with respect to macroscopic tensile stress

Figure 16 -Acoustic emission activity map during the tensile test

For better visualization of the zones of the welded joint featuring a high concentration of cracks, the AE event distribution along the weld is plotted in Figure 16 as a function of the tensile stress. It can be seen from this map that the first zone with a high crack concentration is detected when the FSW joint is subjected to a tensile stress of 77 MPa. Figure 16-b) also shows that the zones with a high crack concentration appear at various levels of the tensile stress, and these “hot” areas may be associated with crack nucleation.

4 Correlation between results

4.1 Mechanical behavior versus AE activity

In this section, the macroscopic mechanical behavior of the welded joint is compared to the AE activity generated during the test. The evolution of the energy level associated with each AE event is plotted as a function of the longitudinal deformation (Figure 17).

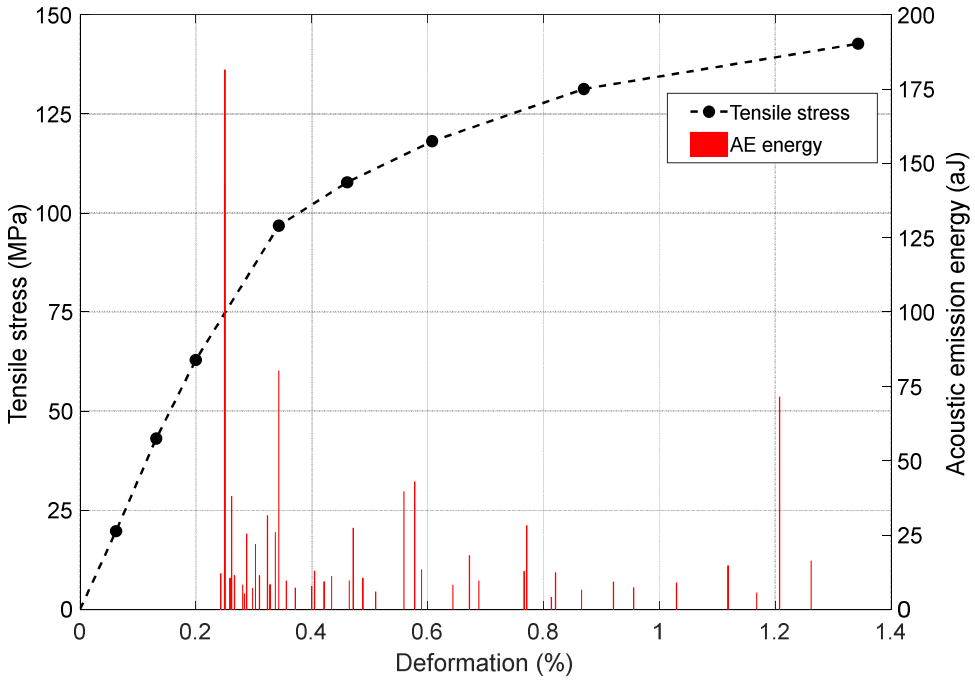

Figure 17 - AE energy analysis to detect the yield strength of the welded joint

It can be seen from this comparison that the very first AE events occur well after the test has started. These results also point out that the highest released acoustic energy level is detected at a stress level of 75 MPa, and at the testing time at which the first crack concentration is detected and localized (see Figure 16). As successfully experienced in a previous study [41], acoustic energy is a feature that helps evaluate, through its evolution, the yield strength of a material or a joint in the present study. Indeed, as long as the yield strength of the material or the assembly is not reached, the latter continues to store mechanical energy. Once reached, the released strain energy is accompanied by transient elastic waves that are highly energetic, which can be related to permanent strain or micro-damage within the material. During the test, the AE software records the wave signals and instantaneously computes and plots the corresponding acoustic energy value. It allows for real-time monitoring of acoustic energy evolution. Based on this evolution plotted in Figure 17, one can point out that the second-highest acoustic energy value is detected when the slope of the macroscopic mechanical behavior curve drastically changes, thus for a tensile stress value of 96 MPa and a longitudinal deformation value of 0.34%.

By comparing the results plotted in Figure 17 and Figure Figure 16, it can be observed that this radical change of slope is accompanied by the detection of crack concentration. In this study, the analysis of the AE activity shows that beyond the detection of first mechanical

damage (crack concentration accompanied with AE events highly energetic), the FSW joint continues to store mechanical energy before reaching its yield strength. This analysis methodology may be used to compare the mechanical efficiency of several welding configurations by evaluating the impact of an early appearance of mechanical damage within the joint on its capacity to have an elastic response.

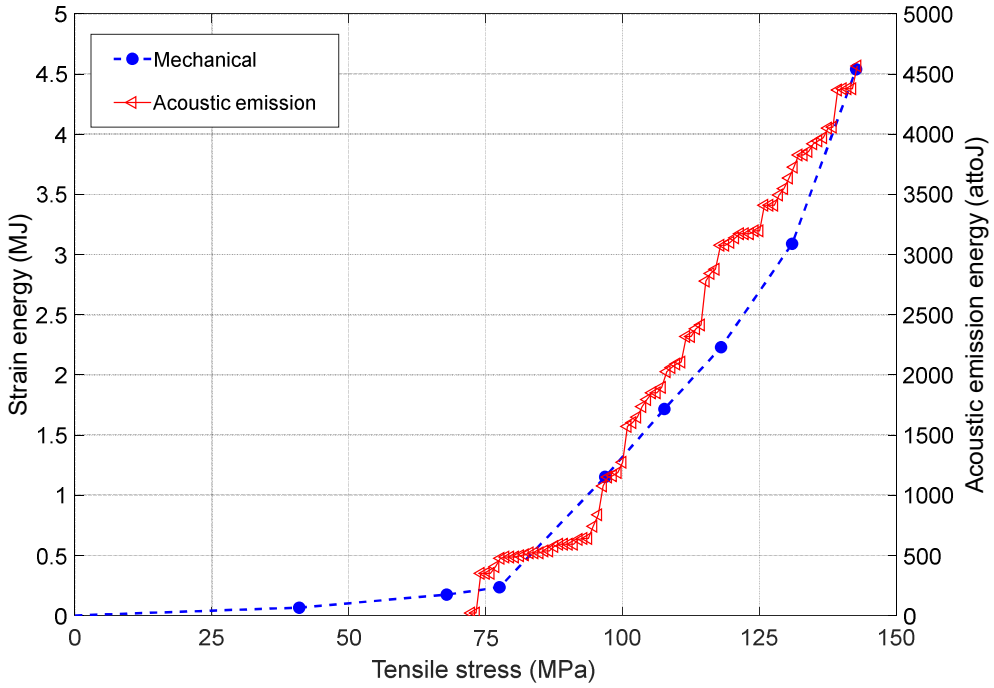

a) Comparison between the evolution of both the strain energy and the acoustic emission energy during the tensile test

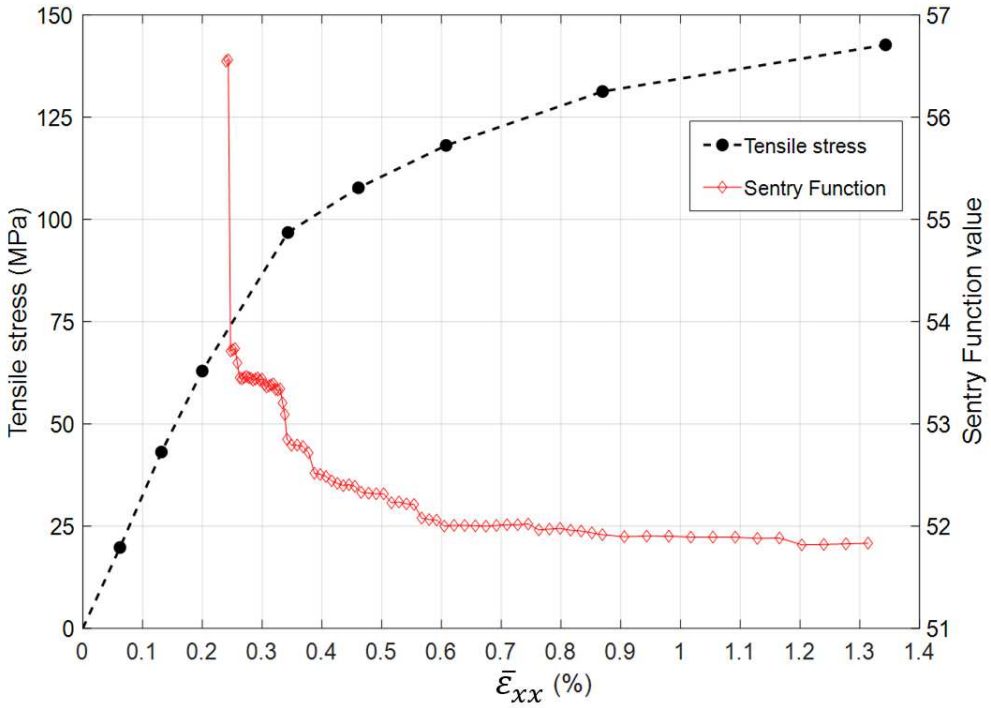

b) Use of the Sentry function to highlight the dependency between the strain energy and the acoustic emission energy during the tensile test

Figure 18 - Sentry function: Dependency between mechanical behavior and AE activity

The evolutions of the mechanical and acoustic emission energies are compared in Figure 18 to investigate in deep the welded joint behavior, in particular beyond its yield strength. One can see in Figure 18-a that for a tensile stress value greater than 78 MPa, the evolutions of the two types of energy show the same trend. There is a ratio of about 1.10^{21} between these two quantities.

As successfully experienced in a previous study [42], the so-called Sentry function allows analyzing in-depth the mechanical behavior of the joint, since it combines both mechanical and acoustic energies. This function is given in equation (6). It involves the logarithm of the ratio between the strain energy $E_s(x)$ and the acoustic energy $E_a(x)$, where x is the test-driving variable (usually displacement or strain).

$$f(x) = ln\left[\frac{E_S(x)}{E_a(x)}\right] \quad \text{(Eq.6)}$$

The Sentry function f(x) is divided into four distinct portions, and each one describes a particular signature of the mechanical behavior of the material (or the joint in the present study). Additional information on this Sentry function can be found in [42, 44]. By analyzing

the results from Figure 18-b, it can be seen that the first stage of the Sentry function is characterized by the sudden release of the strain energy. Following this stage, one can notice some abrupt drops in the Sentry function. Each of them is associated with a sudden release of one part of the strain energy that was stored previously. This sudden release of mechanical energy is accompanied by the generation of acoustic waves with a high level of energy. These results also show that before each abrupt drop in the Sentry function, the joint exhibits an energy-storing phase.

4.2 Initial state of the internal structure versus localization of the AE events

In this section, the main objective is to highlight the correlation between the initial state of the FSW joint and the localization of the very first cracks. In practice, it consists in comparing the results of the X-ray microtomography analysis with those obtained with acoustic emission (see Figure 19).

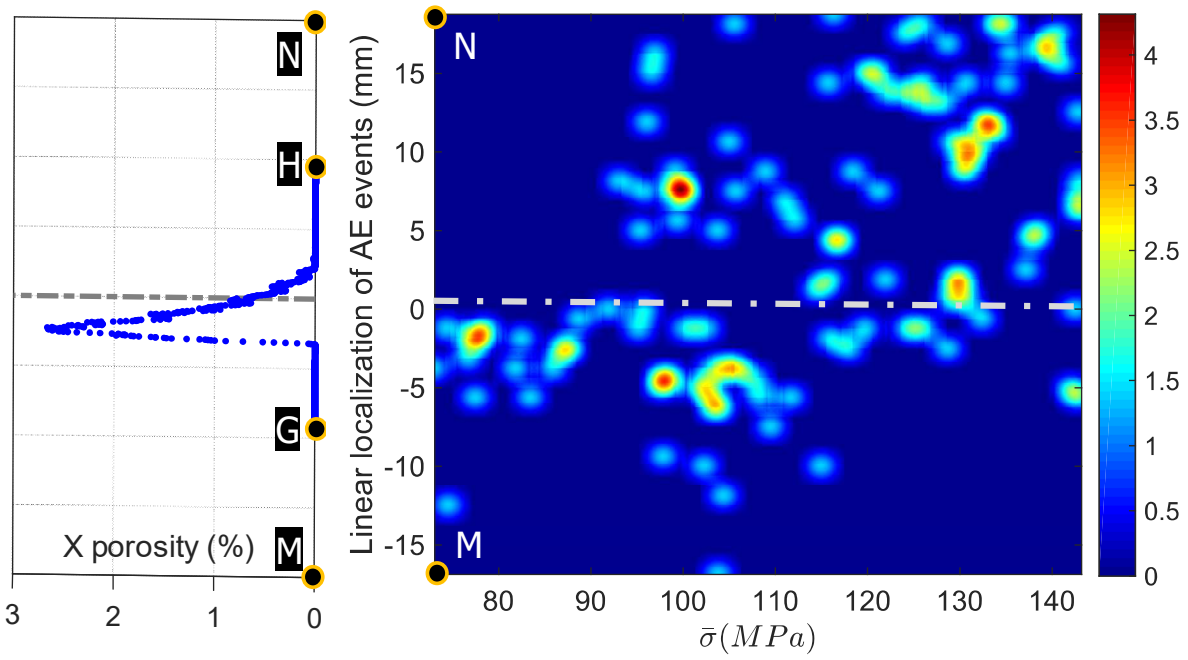

a) Porosity distribution along the $\vec{x}$-direction

b) Linear localization of AE events concentration as a function of applied tensile stress

Figure 19 - X-ray microtomography versus AE: Localization of initial defects versus very first AE events

Results from the X-ray microtomography analysis show a high concentration of initial defects close to the center of the specimen (along the longitudinal axis). As stated in Section 3.4 above, the results from the AE activity (Figure 19-b) show that the very first crack sources are located in the lower half of the joint. This good correlation between the results allows stating

that the first crack sources are caused by the weakness zones detected in the initial state of the welded joint.

In addition to the previous analysis of the experimental results (see Figure 19), the size effect of the initial defect (Figure 20-a) on the acoustic signature of the resulting event is analyzed. This signature is expressed in terms of AE energy (Figure 20-b). The results lead us to state that the bigger the initial defect, the higher the corresponding AE energy level.

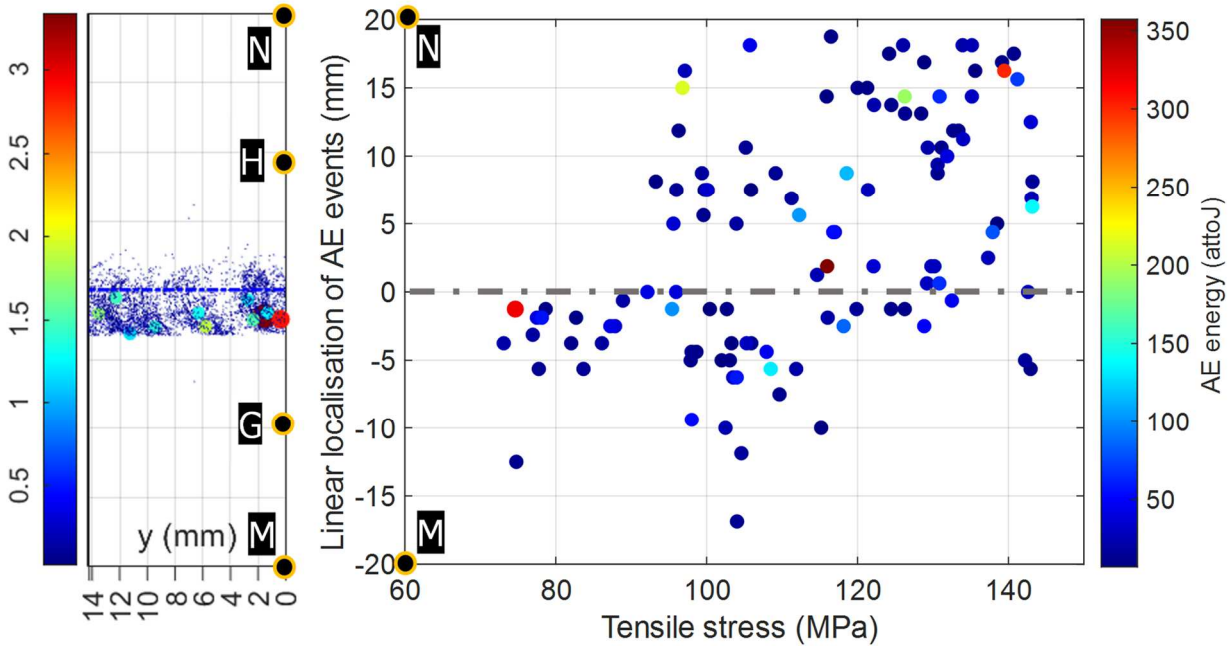

a) Initial defects distribution projected in the XY plane

b) Mono-parametric analysis of AE activity during the tensile test: linear localization of AE events as a function of acoustic energy of the AE signal

Figure 20 - X-ray microtomography vs AE: Localization of initial defects versus AE energy of the very first events

4.3 AE signature of damage mechanisms

As successfully experienced in previous studies [41, 42, 43] the k-means++ clustering algorithm is used to perform an unsupervised classification of the AE events to allow the number of cracking mechanisms (based on the optimal number of clusters) and their crack acoustic signatures to be identified. The optimal number of clusters is statistically determined based on the values of two clustering evaluation indices [42, 43]: the Davies-Bouldin index (DB) and the Silhouette Coefficient (SC).

In the present study, seven AE features (amplitude, rise-time, counts, energy, duration, centroid frequency, and peak frequency) were selected in the clustering process. This optimal number of clusters led to a value of 0.61 for the DB index and 0.71 for the SC index. With these values, the clusters are dense and well separated, which corresponds to the standard concept of cluster. In general, an SC index value greater than 0.6 ensures that the clustering is of sufficient quality. As a result of the clustering process, similar AE events in terms of features can be statistically gathered into four clusters. This means that four cracking mechanisms with different acoustic signatures can be identified from the AE activity of the welding joint.

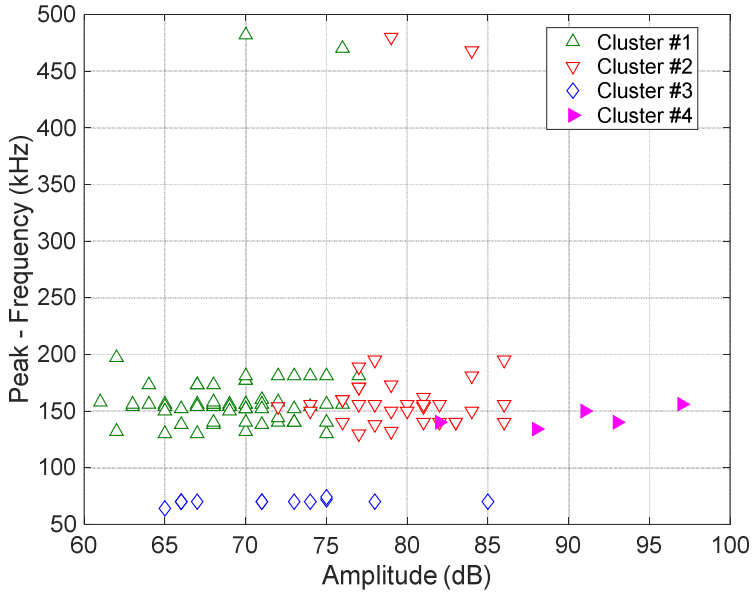

a) Cracking signatures based on the values of peak frequency and amplitude of the AE signal

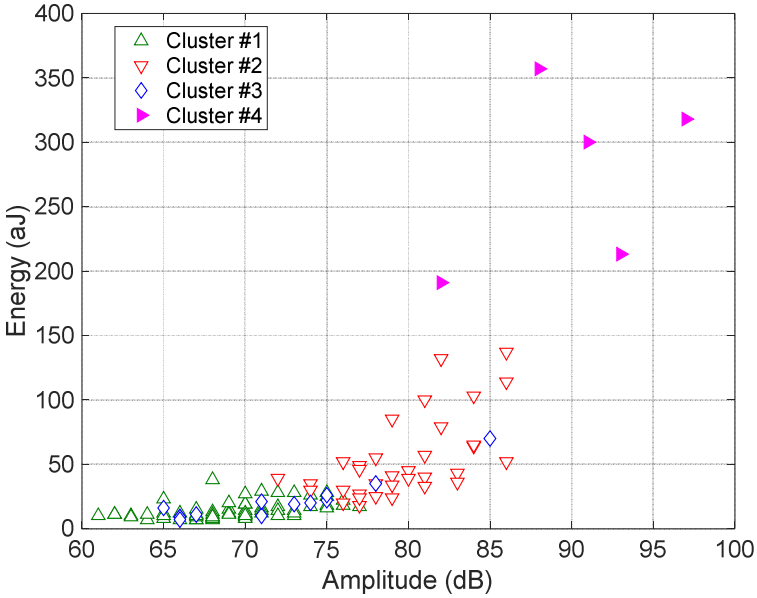

b) Cracking signatures based on the values of energy and amplitude of the AE signal

Figure 21 - AE signatures of the cracking mechanisms

Figure 21 proposes a projection of the four clusters onto a two-dimensional plot. The cluster analysis of the AE events enables us to represent the four clusters either in the peak frequency-amplitude coordinate system (see Figure 21-a) or in the energy-amplitude one (see Figure 21-b), the idea being to get the best separation of the clusters. One can conclude from these results that three main clusters (#1, #2, and #4) can be selected. They are comprised of AE events with a peak frequency value lying between 100 and 250 kHz. This interval falls within the frequency range where the AE sensors that were used are very sensitive. The bounds of these clusters are consequently deduced from the amplitude levels of the AE events.

To complete this analysis of the cracking mechanisms within the FSW joint, the clusters that were previously identified are used in the plot of the linear localization of the AE events (between the two sensors and along the x-axis, Figure 1) as a function of the tensile stress (Figure 22).

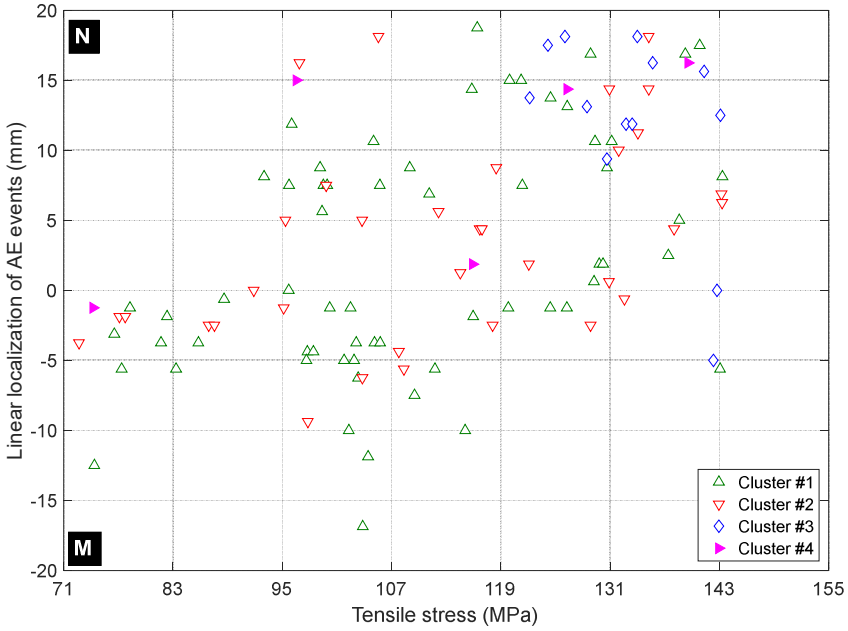

Figure 22 - 1D-localization of cracking mechanisms within the welded joint and during the tensile test

It can be seen from Figure 22 that the very first AE events that are detected belong to clusters #2 and #4. They are characterized by an amplitude greater than around 77 dB and an energy

level greater than around 35 aJ (attojoule). Based on the localization of these two first events and by comparing Figure 22 and Figure 20, one can see that the AE event of cluster#4 is certainly caused by the cracking of the biggest initial defect.

Figure 21 shows that cluster#4 gathers all AE events that exhibit an acoustic energy level greater than around 200 aJ. The linear localization of these events (Figure 22) is in good agreement with the acoustic analysis presented in Figure 20 (focused on events with an energy level greater than 200 aJ). Besides, one can see by comparing Figure 20, Figure 22, and Figure 17 that the AE events of cluster #4 appear at specific moments of the joint mechanical response. They can be due to macroscopic changes in the internal structure of the welded joint.

Figure 22 shows the nucleation of AE events with low amplitude (cluster#1) in the vicinity of those of cluster#2. In the current state of the AE analysis, results from Figure 22 tend to show that at any location in the welded joint AE events of cluster#2 appear before those of cluster#1. Based on these analyses, the AE events of cluster#1 could be due to micro-cracking and, those of cluster#2 be related to macro cracking or crack nucleation. Events of cluster#4 could be associated with crack initiation.

Figure 23 shows how the monitoring of AE events that are characterized by particular acoustic signatures (clusters #2 and #4) can help to predict where the failure zone of the specimen will potentially be located. It provides information about the evolution of the cracked area as a function of the applied tensile stress. As previously highlighted by the analysis of both the strain fields (Figure 13) and AE activity (Figure 20) the very first concentration of deformation is located less than 5 mm from the center (welding line) of the specimen and exhibits the very first AE events (Figure 22 and Figure 23-a) that are characterized by particular acoustic signatures in terms of amplitude, energy, and peak frequency levels (Figure 21). The monitoring of these particular AE events during the test allows showing how the cracked length (based on projected AE events localizations) spreads over the welding line delimited by the two AE sensors (Figure 23). Figure 23-b and Figure 23-c show that some AE events are located in areas where no notable deformations are detected on both investigated surfaces. These AE events are probably due to cracks located either within the specimen volume or on the surface of the aluminum alloy sheet AA2024 since the AE sensors are fitted on this material.

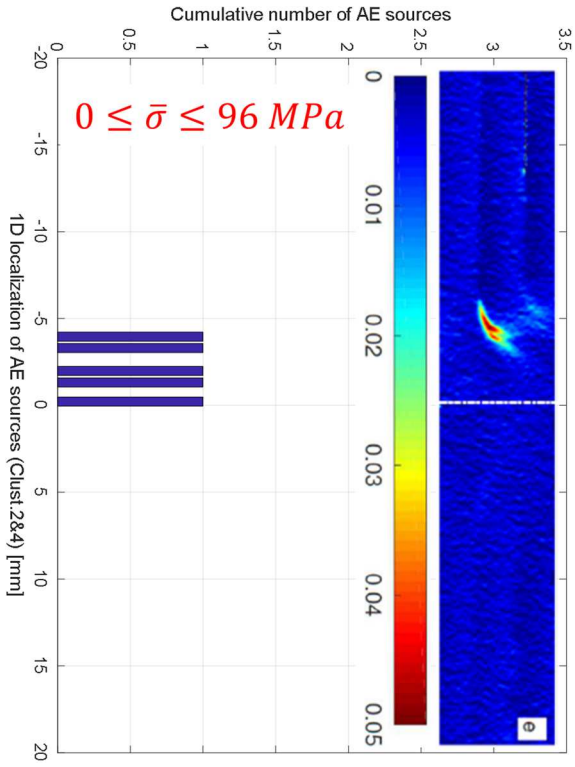

a) Monitoring of AE events with specific signatures and comparison with strain field (ε_{xx} [in ***µdef***])

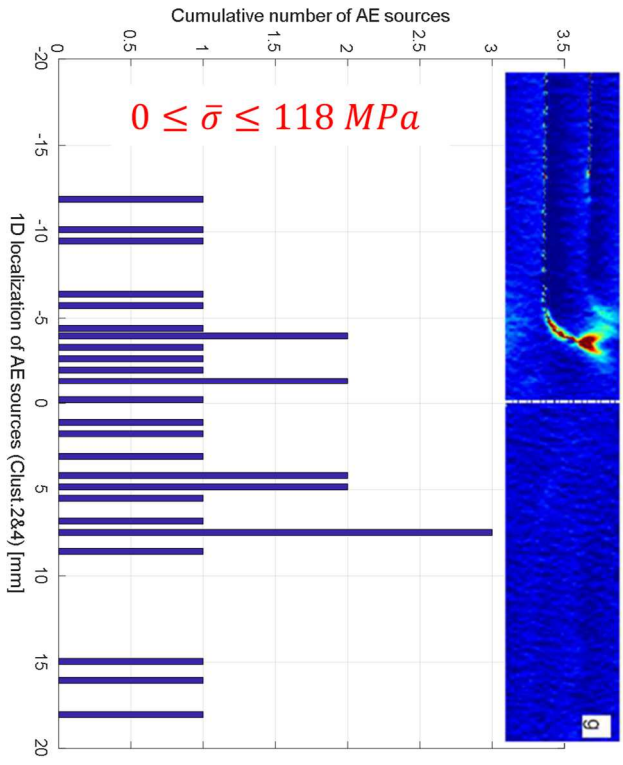

b) Monitoring of AE events with specific signatures and comparison with strain field (ε_{xx} [in ***µdef***])

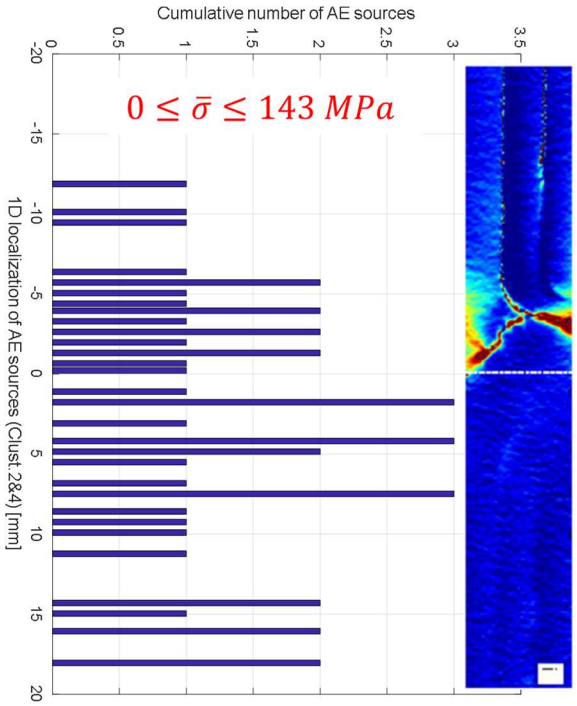

c) Monitoring of AE events with specific signatures and comparison with strain field(ε_{xx} [in ***µdef***]) at specimen failure

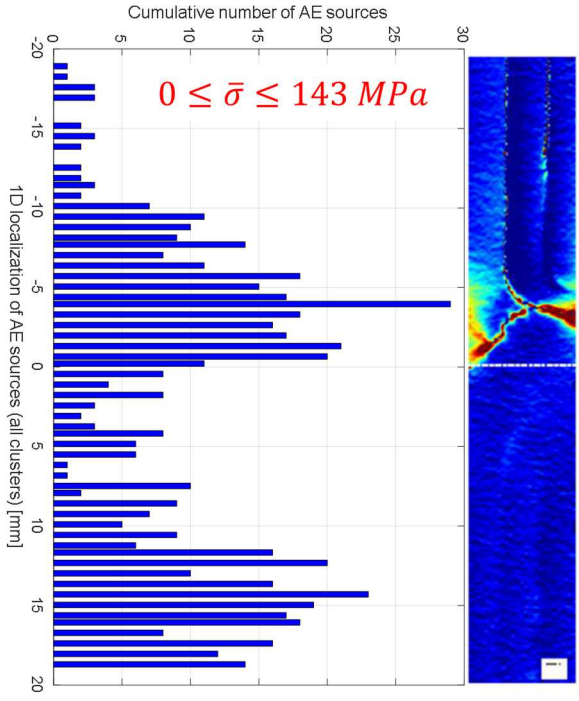

d) Monitoring of AE events and comparison with strain map (ε_{xx} [in ***µdef***]) at specimen failure

Figure 23-Monitoring of AE events and comparison with the corresponding local strain field during the tensile test. The color bar associated with Figure 23-a remains valid for all the deformation maps (ε_{xx} [in ***μdef***]) shown in the other figures (b, c, d).

Figure 24 shows, that when the joint fails, the strain field (ε_{xx}) distribution on both the lateral and the front faces as well as the AE events (all clusters) localizations along the welded joint. The presence of a band perpendicular to the sample with very low ε_{xx} value (dark blue) is visible. This can be explained as follows: looking in Figure 5-a, one can see that during the mixing of the three alloy sheets, the AA7075 alloy moved to the contact with the tool shoulder, removing thus the part of the AA6061 alloy located in the vicinity of the pin. When analyzing Figure 11, one can see that the AA7075 and AA6061 alloys exhibit very different mechanical behavior. Thus, based on the macroscopic stress level of our welded sample, the AA7075 alloy remains in its elastic domain (very small deformation ε_{xx}) while the AA 6061 one is fully in its plastic domain, with a stress value in the x-direction of about 65 MPa. This confirms the good correlation between the experiment results. Since the AE technique allows real-time monitoring of the cracking mechanisms it could be helpful in further experimental works for the identification of the optimal welding process parameters.

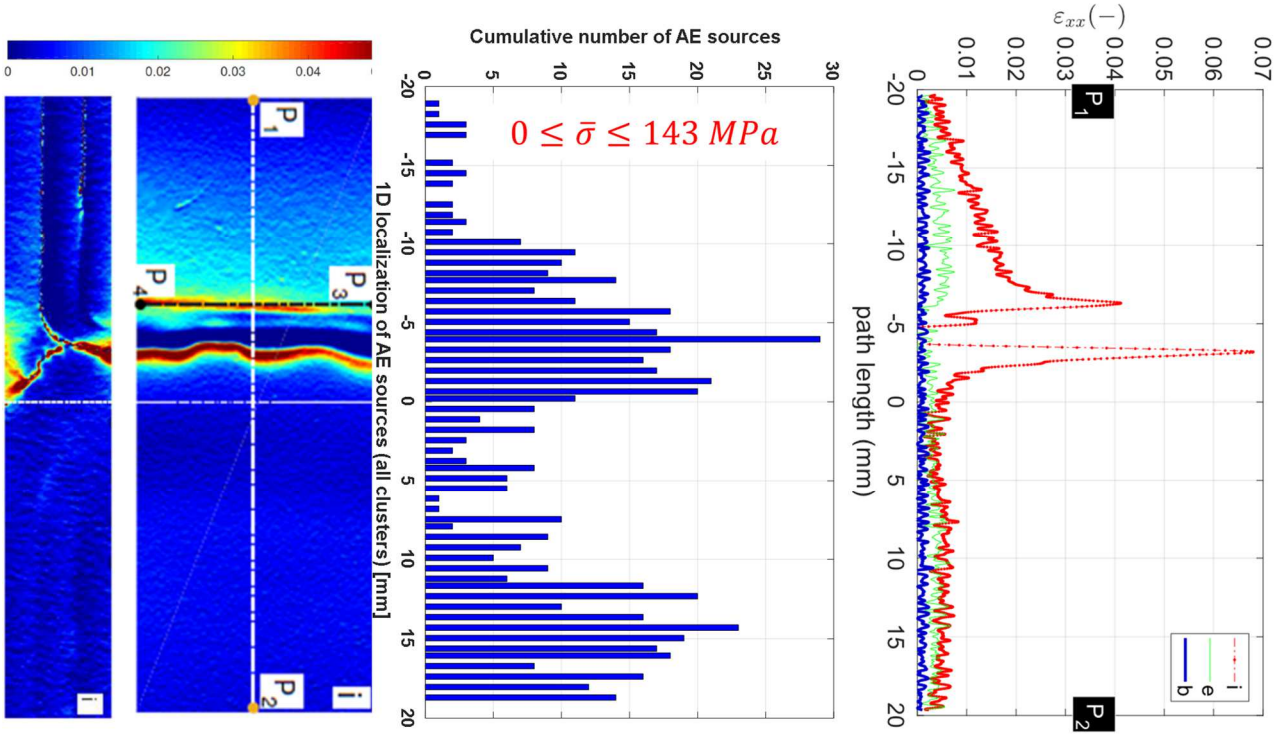

Figure 24 – Specimen fracture: strain field map (ε_{xx} [in ***μdef***]) compared with AE events distribution

5 Conclusions

FSW process was used to weld three superimposed aluminum alloy sheets, namely AA6061, AA7075, and AA2024 (from top to bottom). Three samples were tested with good repeatability but results from only one sample were presented due to the richness of the experimental data. The experimental results show that under tensile loading, the strength of the welded assembly is about 40% lower than that of the configuration made up of three superimposed but non-welded alloy sheets. This relatively low effectiveness compared to that of butt-welded joints is mainly caused by the defects created during the assembling process. Even though the current work is not aimed at identifying the optimal parameters of the welding process, it brings to light how important it is to simultaneously use various experimental techniques for a better understanding of the phenomena that occur during the mechanical loading of the joint.

The use of X-ray micro-computed tomography seems to be essential for a good understanding of the internal structure of the joint before being subjected to mechanical loading. Indeed, it highlighted the mixing of the alloy sheets after manufacturing on the one hand and enabled us

to evaluate both the distribution and the dimensional characteristics (shape, location, etc.) of the defects on the other hand. This analysis shows that the majority of the defects are characterized by an equivalent diameter lower than 0.2 mm and a rather spherical shape (sphericity rates larger than 0.5). The defects that are characterized by both a rate of sphericity lower than 0.4 and an equivalent diameter greater than 0.6 mm have a very particular shape. Such defects have been already observed in previous studies. In the present study, results show that their locations are correlated with micro-cracks initiation and damage evolution. Two perpendicular faces of the specimen were marked by using periodic patterns, namely a checkerboard, in order to ensure a high quality of the displacement and strain fields measurement by processing the pattern images shot during the test by a spectral method like the Localized Spectrum Analysis. The experimental results confirm the ability of this non-contact measurement technique to detect very early the appearance of strain concentrations on the two surfaces of the specimen that were investigated at the same time. The findings highlight a good correlation between the strain concentration zones and those characterized by a high density of defects, as also observed from the microtomography results analysis. Moreover, the presence of a significant density of defects within the FSW joint is undoubtedly the cause of the early cracking of the assembly, and thus also the cause of the quite low strength of the weld.

By analyzing the localization of AE events within the FSW joint, it can be seen that cracking starts at the lower half of the joint before spreading throughout the assembly. Moreover, the monitoring of the acoustic energy evolution during the mechanical test helped evaluate the yield strength of the welded joint. AE results were also compared with those obtained with the computed microtomography analysis in order to highlight the correlation between the initial state of the FSW joint and the localization of the very first cracks. This comparison allowed stating that the first crack sources were caused by the weakness zones detected at the initial state of the welded joint. In a deep analysis of the AE results, the k-means++ clustering algorithm was used to perform an unsupervised classification of the AE events, which led the number of cracking mechanisms and their crack acoustic signatures to be identified. The findings were that three main mechanisms governed the damage evolution of the studied FSW joint. The acoustic signature of each cracking mechanism was defined by a pair of values (peak frequency, amplitude), each within a specific range. The results highlight a good correlation between the AE results with those from the strain analysis. Thus, the ability of the AE technique to provide real-time results should be helpful to identify the optimal welding process parameters in further experimental studies. It should also be relevant to investigate the

evolution of the defects distribution in the bulk of such FSW joints by performing microtomography analysis at several levels of the mechanical loading. The experimental strategy developed in the framework of this study will be followed in our future works to identify the optimal welding parameters, thus optimizing the in-service life of the joint.

6 References

[1] France: CO2 Country Profile. https://ourworldindata.org/co2/country/france

[2] N. Leconte, B. Bourel, F. Lauro, C. Badulescu, E. Markiewicz, Strength and failure of an aluminum/PA66 self-piercing riveted assembly at low and moderate loading rates: Experiments and modeling, Int. J. Impact Eng. 142 (2020) https://doi.org/10.1016/j.ijimpeng.2020.103587.

[3] G. Zhang, H. Zhao, X. Xu, G. Qiu, Y. Li, Z. Lin, Metallic bump assisted resistance spot welding (MBaRSW) of AA6061-T6 and Bare DP590: part II-joining mechanism and joint property, J. Manuf. Process. 44 (2019) 19–27, https://doi.org/10.1016/j. jmapro.2019.05.041.

[4] W.M. Thomas, E.D. Nicholas, J.C. Needham, M.G. Murch, P. Temple-Smith, C.J. Dawes, Friction welding, United States Pat. 5,460,317 (1991). https://patents. google.com/patent/US5460317.

[5] D. Camilleri, D. Micallef and P. Mollicone, Thermal Stresses and Distortion Developed in Mild Steel DH36 Friction Stir-Welded Plates: An Experimental and Numerical Assessment, J. Therm. Stresses, 38(5), (2015) 485-508, DOI: 10.1080/01495739.2015.1015856

[6] T. Liyanage, J. Kilbourne, A.P. Gerlich, T.H. North, Joint formation in dissimilar Al alloy/steel and Mg alloy/steel friction stir spot welds, Sci. Technol. Weld. Join. 14 (2009) 500–508, https://doi.org/10.1179/136217109X456960

[7] R.P. Mahto, S.K. Pal, Friction stir lap welding of thin AA6061-T6 and AISI304 sheets at different values of pin penetrations, ASME 2018 13th Int. Manuf. Sci. Eng. Conf. MSEC 2018, 2018, https://doi.org/10.1115/MSEC2018-6590

[8] Z. Shen, Y. Chen, M. Haghshenas, T. Nguyen, J. Galloway, A.P. Gerlich, Interfacial microstructure and properties of copper clad steel produced using friction stir welding versus gas metal arc welding, Mater. Charact. 104 (2015) 1–9, https://doi. org/10.1016/j.matchar.2015.02.022.

[9] Almigdad B. Ibrahim and Fadi Al-Badour and Akeem Yusuf Adesina and Nesar Merah , Effect of process parameters on microstructural and mechanical properties of friction stir diffusion cladded ASTM A516-70 steel using 5052 Al alloy, J. Manuf. Processes 34 (2018) 451-462. DOI:10.1016/J.JMAPRO.2018.06.020

[10] Noor Zaman Khan, Arshad Noor Siddiquee, Zahid A. Khan, Suha K. Shihab, Investigations on tunneling and kissing bond defects in FSW joints for dissimilar aluminum alloys, J. Alloys Compd. 648 (2015) 360-367. https://doi.org/10.1016/j.jallcom.2015.06.246.

[11] Raju Prasad Mahto, Ravi Kumar, Surjya Kanta Pal, Characterizations of weld defects, intermetallic compounds and mechanical properties of friction stir lap welded dissimilar alloys, Mater. Charact. 160 (2020) https://doi.org/10.1016/j.matchar.2019.110115

[12] Monica Daniela Iordache, Claudiu Badulescu, Malick Diakhate, Marius Adrian Constantin, Eduard Laurentiu Nitu, Younes Demmouche, Matthieu Dhondt, Denis Negrea, A numerical strategy to identify the FSW process optimal parameters of a butt-welded joint of quasi-pure copper plates: modeling and experimental validation, Int. J. Adv. Manuf. Technol. 115 (2021) 2505–2520. https://doi.org/10.1007/s00170-021-07296-9

[13] Y.C. Lim, Mechanical Properties and Microstructural Characterization of a Multilayered Multipass Friction Stir Weld in Steel. In: Mishra R., Mahoney M.W., Sato Y., Hovanski Y., Verma R. (eds) Friction Stir Welding and Processing VII. Springer, Cham. (2013) https://doi.org/10.1007/978-3-319-48108-1_9

[14] M. Geyer, V. Vidal, T. Pottier, C. Boher and F. Rézaï-Aria, Investigations on the material flow and the role of the resulting hooks on the mechanical behaviour of dissimilar friction stir welded Al2024-T3 to Ti-6Al-4V overlap joints, J. Mater. Process. Technol. 292, (2021), yyy-yyy, https://doi.org/10.1016/j.jmatprotec.2021.117057

[15] Kaifeng Wang, Haris Ali Khan, Zhiyi Li, Sinuo Lyu, Jingjing Li, Micro friction stir welding of multilayer aluminum alloy sheets, J. Mater. Process. Technol., 260 (2018) 137-145. https://doi.org/10.1016/j.jmatprotec.2018.05.029

[16] R.F. Hamade, A.M.R. Baydoun, Nondestructive detection of defects in friction stir welded lap joints using computed tomography, Materials & Design, Volume 162, 2019, Pages 10-23, https://doi.org/10.1016/j.matdes.2018.11.034

[17] M. Dhondt, I. Aubert, N. Saintier, J.M. Olive, Mechanical behavior of periodical microstructure induced by friction stir welding on Al–Cu–Li 2050 alloy, Mater. Sci. Eng., A,644,(2015), 69-75, https://doi.org/10.1016/j.msea.2015.05.072

[18] D. Texier, F. Atmani, P. Bocher, F. Nadeau, J. Chen, Y. Zedan, N. Vanderesse, V. Demers, Fatigue performances of FSW and GMAW aluminum alloys welded joints: Competition between microstructural and structural-contact-fretting crack initiation, Int. J. Fatigue, 116,(2018), 220-233, https://doi.org/10.1016/j.ijfatigue.2018.06.020

[19] S.A. Nikulin, S.V. Dobatkin, V.G. Khanzhin, S.O. Rogachev, and S.A. Chakushin, Submicrocrystalline structure and inclusions on the deformation and failure of aluminum alloys and titanium, Met. Sci. Heat Treat., 51 (2009) 208-217

[20] S. Senthil Kumar, S. Denis Ashok, Development of Acoustic Emission and Motor Current Based Fuzzy Logic Model for Monitoring Weld Strength and Nugget Hardness of FSW Joints, Procedia Eng., 97 (2014) 909-917. https://doi.org/10.1016/j.proeng.2014.12.366.

[21] A. Rastegaev, M.L. Linderov, D.L. Merson, M.A. Afanasyev and A.V. Danyuk, Monitoring of fracture of welded joints in hazardous facilities by acoustic emission under

static and cyclic loadings, Indian J. Sci. Technol. 8 (35) (2015) 1-7. doi: 10.17485/ijst/2015/v8i36/90555

[22] A. Boșneag, M. A. Constantin and E. L. Nitu, Numerical simulation of Friction Stir Welding of three dissimilar aluminium alloys, IOP Conf. Ser.: Mater. Sci. Eng. 564 012033 (2019). doi:10.1088/1757-899X/564/1/012033

[23] A. Boșneag, M.A. Constantin, E. Nițu and M. Iordache, Friction Stir Welding of three dissimilar aluminium alloy used in aeronautics industry, IOP Conf. Series: Materials Science and Engineering 252 (2017) 012041 doi:10.1088/1757-899X/252/1/012041

[24] J.-Y. Buffière, E. Maire, J. Adrien, J.-P. Masse, E. Boller, In situ experiments with X ray tomography: an attractive tool for experimental mechanics, Exp. Mech. 50 (2010) 289–305.

[25] C. Petit, E.Maire, S. Meille, J. Adrien, Two-scale study of the fracture of an aluminum foam by X-ray tomography and finite element modeling, Mater. Des. vol. 120 (2017) 117–127

[26] H. Toda, T. Ohgaki, K. Uesugi, T. Kobayashi, N. Kuroda, T. Kobayashi, M. Niinomi, T.Akahori, K. Makii, Y. Aruga, Quantitative assessment of microstructure and its effect on compressive behavior of aluminum foams via high-resolution synchrotron X-ray tomography, Metall. Mater. Trans. A 37 (2006) 1211–1219. https://doi.org/10.1007/s11661-006-1072-0

[27] Kak, A. C.; Slaney, M. Principles of Computerized Tomographic Imaging; Society for Industrial and Applied Mathematics: Philadelphia (2001)

[28] M. Sutton, J.J. Orteu, and H. Schreier. Image Correlation for Shape, Motion and Deformation Measurements. Basic Concepts, Theory and Applications. Springer (2009)

[29] M. Grédiac, B. Blaysat, and F. Sur. *On the optimal pattern for displacement field measurement: random speckle and DIC, or checkerboard and LSA?* Exp. Mech., 60(4) (2020) 509-534. https://doi.org/10.1007/s11340-019-00579-z

[30] J.L. Piro and M. Grédiac. Producing and transferring low-spatial-frequency grids for measuring displacement fields with moiré and grid methods. Exp. Tech., 28(4) (2004) 23-26. DOI: 10.1111/j.1747-1567.2004.tb00173.x

[31] F. Sur, B. Blaysat, and M. Grédiac. Determining displacement and strain maps immune from aliasing effect with the grid method. Opt. Lasers Eng., 86 (2016) 317-328. https://doi.org/10.1016/j.optlaseng.2016.06.010

[32] M. Grédiac, B. Blaysat, and F. Sur. Extracting displacement and strain fields from checkerboard images with the localized spectrum analysis. Exp. Mech., 59(2) (2019) 207-218. https://doi.org/10.1007/s11340-018-00439-2

[33] NIH National Institute of Health, Image J [in line]. Available on: http://imagej.nih.

[34] M. Sezgin, Survey over Image Thresholding Techniques and Quantitative Performance Evaluation. J. Electron. Imaging. 13 (2004) 146–165. DOI: 10.1117/1.1631315.

[35] A. Rosenfeld, P. De La Torre, Histogram Concavity Analysis as an Aid in Threshold Selection. IEEE Trans. Syst. Man Cybern. 13 (1983) 231–235 DOI:10.1109/TSMC.1983.6313118.

[36] N. Otsu, A Threshold Selection Method from Gray-Level Histograms. IEEE Trans. Syst. Man Cybern. 9 (1979) 62–66. DOI: 10.1109/TSMC.1979.4310076.

[37] R.F. Hamade, A.M.R. Baydoun, Nondestructive detection of defects in friction stir welded lap joints using computed tomography, Mater. Des. 162 (2019) 10-23. https://doi.org/10.1016/j.matdes.2018.11.034.

[38] Dimitri Jacquin, Gildas Guillemot, A review of microstructural changes occurring during FSW in aluminium alloys and their modelling, J. Mater. Process. Technol., 288 (2021) https://doi.org/10.1016/j.jmatprotec.2020.116706

[39] G. Lehmann, D. Legland, U.M.R. Efficient N-Dimensional Surface Estimation Using Crofton Formula and Run-length Encoding. Insight J. 2012, 2, 1–11.

[40] H. Wadell, Volume, Shape, and Roundness of Quartz Particles. J. Geol. 43(3) (1935) 250–280. DOI: 10.1086/624298

[41] J. Destouesse, M. Diakhate, C. Badulescu, D. Thévenet, M. Stackler, W. Albouy, N. Carrere, Cluster analysis of acoustic emission data to investigate the damage evolution in modified scarf joint under bi-axial loading, J. Adhes. 96 (2018) 969–987. doi:10.1080/00218464.2018.1552854

[42] M. Diakhate, E. Bastidas-Arteaga, R. Moutou Pitti, F. Schoefs, Cluster analysis of acoustic emission activity within wood material: Towards a real-time monitoring of crack tip propagation, Eng. Fract. Mech. 180 (2017) 254–267. doi:10.1016/j.engfracmech.2017.06.006

[43] L. Li, S.V. Lomov, X. Yan, V. Carvelli, Cluster analysis of acoustic emission signals for 2D and 3D woven glass/epoxy composites, Compos. Struct. 116 (2014) 286–299. doi:10.1016/j.compstruct.2014.05.023.

[44] A.A. Bakhtiary Davijani, M. Hajikhani, M. Ahmadi, Acoustic Emission based on sentry function to monitor the initiation of delamination in composite materials, Mater. Des. 32 (2011) 3059–3065. doi:https://doi.org/10.1016/j.matdes.2011.01.010.